Reviews in Mineralogy & Geochemistry
Vol. 78 pp. 219-269, 2014

Analytical Transmission Electron Microscopy

Rik Brydson[1], Andy Brown[1], Liane G. Benning[2]

[1]Institute for Materials Research
[2]School of Earth and Environment
University of Leeds
Leeds, LS2 9JT, United Kingdom

R.M.Drummond-Brydson@leeds.ac.uk

Ken Livi

High-Resolution Analytical Electron Microbeam Facility
Integrated Imaging Center
Department of Earth and Planetary Sciences
Johns Hopkins University
Baltimore, Maryland 21218, U.S.A.

INTRODUCTION

Analytical transmission electron microscopy (TEM) is used to reveal sub-micrometer, internal fine structure (the *microstructure* or *ultrastructure*) and chemistry in minerals. The amount and scale of the information which can be extracted by TEM depends critically on four parameters; the resolving power of the microscope (usually smaller than 0.3 nm); the energy spread of the electron beam (of the order of an electron volt, eV); the thickness of the specimen (almost always significantly less than 1 μm), and the composition and stability of the specimen. An introductory text on all types of electron microscopy is provided by Goodhew et al. (2001), while more detailed information on transmission electron microscopy may be found in the comprehensive text of Williams and Carter (2009).

INTRODUCTION TO ANALYTICAL TRANSMISSION ELECTRON MICROSCOPY (TEM)

Basic design of transmission electron microscopes (TEM)

The two available modes of TEM—CTEM and STEM—differ principally in the way they address the specimen. Conventional TEM (CTEM) is a wide-beam technique, in which a close-to-parallel electron beam floods the whole area of interest and the image (or diffraction pattern), formed by an imaging (objective) lens after the thin specimen from perhaps 10^6-10^7 pixels on a digital camera, is collected in *parallel*. Scanning TEM (STEM) deploys a fine focused beam, formed by a probe-forming lens before the thin specimen, to address each pixel (here, a dwell point) in *series* and form a sequential image as the probe is scanned across the specimen. Figures 1 and 2 summarize these different instrument designs; here it should be noted that many modern TEM instruments are capable of operating in both modes, rather than being instruments dedicated to one mode of operation.

In both types of instrument analytical information from a small region is usually collected using a focused beam. The smallest region from which an analysis can be collected is defined by the diameter of this beam and hence the corresponding through-thickness volume in the

1529-6466/14/0078-0006$10.00 http://dx.doi.org/10.2138/rmg.2014.78.6

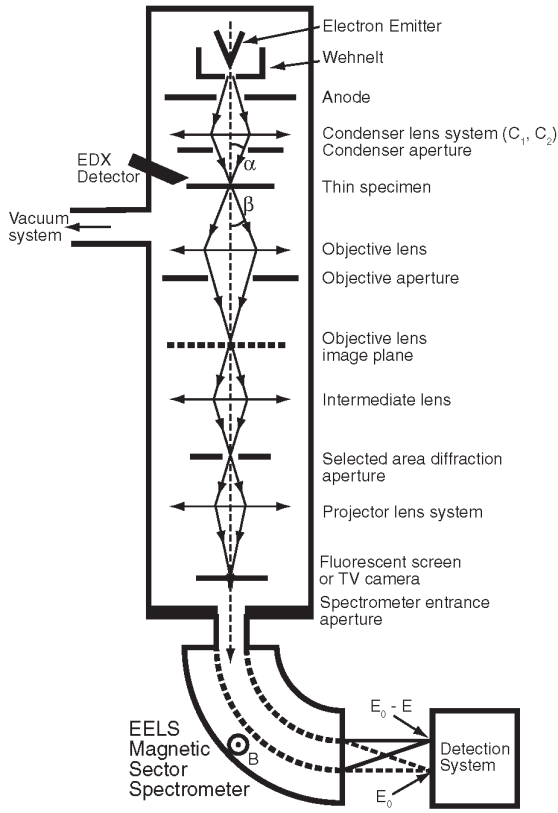

Figure 1. Schematic diagram of the layout of an analytical conventional transmission electron microscope (CTEM) fitted with an energy dispersive X-ray (EDX) detector and an electron energy loss (EEL) spectrometer (after Brydson 2001, 2011). α and β denote the convergence and collection angles. E_o is incident beam energy, E is the energy loss of the fast electron and B is the magnetic field in the spectrometer.

specimen within which various elastic and inelastic scattering (energy-loss) processes take place.

In both CTEM and STEM, electrons are produced from an electron emitter, focused and collimated into a beam and finally accelerated to a given beam energy. Key instrumental components, which affect the microscope resolution and analytical performance, are:

- the electron emitter which can operate via either a thermionic or field emission mechanism or a combination of the two; field emission provides the brightest, most monochromatic and coherent source of electrons.
- the accelerating voltage (E_o, typically in the range 60-300 kV) and hence incident electron energy; the higher the accelerating voltage the higher the resolution and the larger the sample penetration (although, in certain cases depending on the elements present and their chemical bonding, sample damage via sputtering may be an issue above a certain threshold energy).

In the CTEM (Fig. 1), two or more electromagnetic condenser lenses demagnify the probe to a size typically between a few micrometers and a few nanometers—the excitation of these lenses controls both the beam diameter and the beam divergence/convergence angle. For these

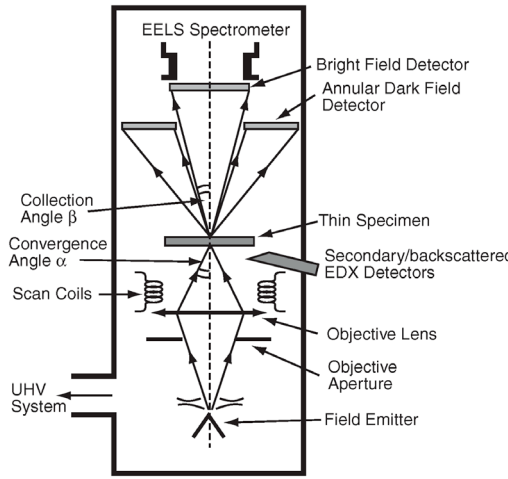

Figure 2. Schematic diagram of the layout of a dedicated analytical scanning transmission electron microscope (STEM) fitted with an energy dispersive X-ray (EDX) detector and an electron energy-loss (EEL) spectrometer (after Brydson 2001, 2011). α and β denote the convergence and collection angles, respectively. Note this is a dedicated UHV STEM configuration with the electron emitter at the base of the microscope for reasons of stability; in the more usual hybrid CTEM/STEM instruments, STEM mode is achieved using the TEM condenser lens system (Fig. 1) which is prior to the specimen and is used to converge a probe which is then scanned across the specimen.

condenser-lens systems the first condenser (C1 or spot size) controls the demagnification of the source, while the second (C2 or intensity) controls the size of the spot at the specimen and hence the beam divergence/convergence.

The specimen is in the form of a thin (< 100 nm) 3 mm diameter disc of either the material itself or the material supported on an electron transparent film. The specimen is usually inserted into the vacuum of the TEM via an airlock and fixed into a side-entry specimen rod that can be translated or tilted (about one or two axes).

In the CTEM (see Fig. 1), the main electromagnetic objective lens forms the first intermediate, real space, projection image of the illuminated specimen area (in the image plane of the lens) as well as the corresponding reciprocal space diffraction pattern (in the back focal plane of the lens). Here the image magnification relative to the specimen is typically 50-100 times. For a given electron emitter and accelerating voltage, the image resolution in CTEM is principally determined by imperfections or aberrations in this objective lens. An objective aperture can be inserted in the back focal plane of the objective lens to limit beam divergence in reciprocal space of the transmitted electrons contributing to the magnified image. Typically there are a number of circular objective apertures ranging from 10 to 100 μm in diameter. The projector lens system consists of a first projector or intermediate lens that focuses on either the objective lens image plane (microscope operating in imaging mode) or the back focal plane (microscope in diffraction mode). The first projector lens is followed by a series of three or four further projector lenses—each of which magnify the image or diffraction pattern by typically up to 20 times. The Selected Area Electron Diffraction (SAED) aperture usually lies in the image plane of one of the projector lenses (due to space considerations) and if projected back to the first intermediate image and hence the specimen effectively allows the selection of a much smaller area (typically ranging from a few tenths of a micron to a few microns) on the specimen for the purposes of forming a diffraction pattern. The overall microscope system can provide a total magnification of up to a few million times on the electron fluorescent microscope

viewing screen or, below this, the camera (either a photographic plate or a phosphor coupled to a two dimensional charge coupled diode (CCD) array).

In the STEM (see Fig. 2), as opposed to CTEM, there is usually only a condenser lens system, which is better called a probe-forming lens; confusingly in a STEM this is often referred to as an objective lens—however, the important distinction from the case of CTEM is that this objective lens lies before the specimen. This lens system is used to form a small diameter (typically a nanometer or less) probe that is serially scanned in a two-dimensional raster across the specimen. At each point the transmitted beam intensity is measured—thus building up a serial image of the specimen. Two intensities are usually recorded: that falling on an on-axis bright field (BF) detector that collects electrons that have undergone relatively small angles of scattering (principally undiffracted, Bragg diffracted and inelastically scattered electrons which gives images equivalent to CTEM BF images), as well as that incident on a high-angle annular dark-field (HAADF) detector that principally collects higher-angle (beyond the diffracted spots) incoherently elastically scattered electrons (so called *Z*-contrast images). In a STEM instrument, the resolution of the scanned image (as well as the analytical resolution described above) is determined largely by the beam diameter generated by the probe-forming lens and this is also limited by lens aberrations. As discussed in the introduction, there are now many hybrid CTEM/STEM instruments, which can operate in both modes.

Interactions between the electron beam and the specimen

The high-energy incident electron beam of the TEM interacts with the sample in a number of ways. Low-angle, coherent elastic scattering (diffraction) of electrons (through 1°-10°) occurs via the interaction of the incident electrons with the electron cloud associated with atoms in a solid—this is used for CTEM and STEM bright field imaging. High-angle, incoherent elastic (back)scattering (through 10-180°) occurs via interaction of the negatively charged electrons with the nuclei of atoms—this is used for STEM dark field imaging. The cross section or probability for elastic scattering varies roughly as the square of the mean atomic number of the sample, whereas inelastic scattering, which provides the analytical signal, generally involves much smaller scattering angles than is the case for elastic scattering; the cross section of inelastic scattering varies linearly with atomic number.

Inelastic scattering of electrons by solids predominantly occurs via four major mechanisms:

1. *Phonon scattering*, where the incident electrons excite phonons (atomic vibrations) in the material. Typically the energy loss is < 1 eV, the scattering angle is quite large (~10°) and for carbon, the average distance between such scattering events—the mean free path, Λ—is ~1 μm. This is the basis for heating of the specimen by an electron beam.

2. *Plasmon scattering*, where the incident electrons excite collective, ''resonant'' oscillations (plasmons) of the valence (bonding) electrons associated with a solid. Here, the energy loss from the incident beam is between 5-30 eV and Λ is ~100 nm, causing this to be the dominant scattering process in electron-solid interactions.

3. *Single-electron excitation*, where the incident electron transfers energy to single atomic electrons resulting in the ionization of atoms. The mean free path for this event is of the order of μm. Lightly bound valence electrons may be ejected from atoms and, if they escape from the specimen surface, may be used to form secondary electron images in scanning electron microscopy (SEM). Energy losses for such excitations typically range up to 50 eV. If inner-shell electrons are removed, the energy loss can be up to keV. For example, the energy loss required to ionize carbon 1*s* (i.e., *K* shell) electrons is 284 eV. The energy loss of the incident beam can be used in electron energy-loss spectroscopy (EELS) analysis and the secondary emissions (e.g., X-ray or Auger electron production; see Fig. 3) produced when the ionized atom relaxes can

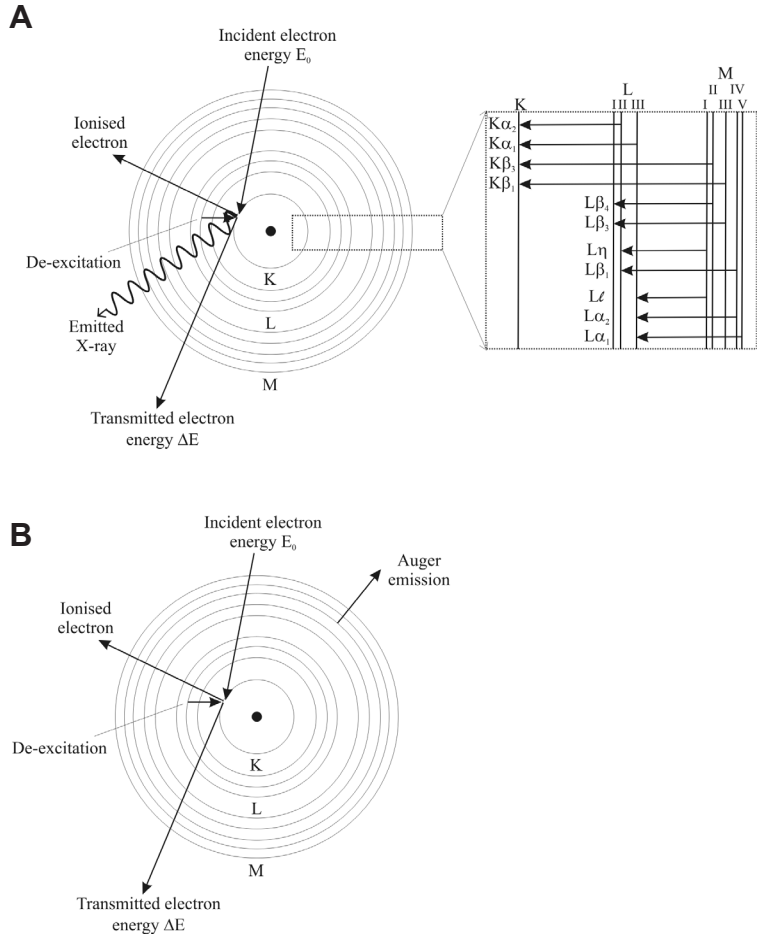

Figure 3. Energy dispersive X-ray analysis in the TEM (after Brydson 2011). De-excitation mechanisms for an atom which has undergone *K*-shell ionization by primary electrons: (A) emission of a characteristic K_α X-ray (the inset details possible ionization processes and emission of X-rays) and (B) emission of a KLM Auger electron.

also be used for analytical purposes in the techniques of either energy dispersive or wavelength dispersive X-ray (EDX/WDX) spectroscopy.

4. *Direct radiation losses*, the principal of which is Bremsstrahlung X-ray emission caused by the deceleration of electrons by the solid; this forms the background in the X-ray emission spectrum upon which are superimposed characteristic X-ray peaks produced by single-electron excitation and subsequent relaxation. The Bremsstrahlung energy losses can take any value and can approach the total incident beam energy in the limit of full deceleration.

Brief review of imaging mechanisms in CTEM and STEM. All TEM images are two dimensional projections of the internal structure of a thin specimen region. In recent years, however, there has been considerable interest in reconstructing the three dimensional nature of the specimen using tomographic techniques (see Weyland and Midgley (2007) in Hutchison

and Kirkland (2007)). Notwithstanding, unless they are STEM EDX or EEL spectrum images or energy filtered CTEM images (see "*EDX and EELS Imaging*" section below), all TEM images are based principally on the elastically scattered components of the incident electron beam although the images may contain some underlying inelastically scattered contribution (Williams and Carter 2009).

There are three basic contrast mechanisms which contribute to all CTEM images:

1. *Mass-thickness contrast*: sample regions (whether amorphous or crystalline) that are thicker or of higher density will scatter the electrons more strongly and hence more electrons will be scattered through high angles and be lost in their passage down the narrow bore of the microscope column so making these areas appear darker in the image.
2. *Diffraction contrast*: crystalline regions of the sample oriented at the Bragg angle for diffraction will excite diffracted beams, which correspondingly reduce the amplitude of the unscattered beam. Insertion of an objective aperture in the back focal plane can accentuate this effect via formation of bright field (BF) images (the unscattered beam selected with diffracting regions appearing dark) or dark field (DF) images (a diffracted beam selected, with diffracting regions appearing bright). Any microstructural feature which changes the corresponding diffraction condition (such as a grain boundary, stacking fault, strain field or a line defect etc.) will, in principle, show up in diffraction contrast.
3. *Phase contrast*: this relies on the interference between the unscattered beam and different diffracted beams to produce an interference pattern (visible at high magnification) which reflects the lattice periodicity; effectively lattice planes and hence atomic positions are imaged but may appear light or dark depending on the microscope conditions (objective lens defocus, beam energy, etc.) and the sample thickness.

Some examples of these three CTEM contrast mechanisms are given in Figure 4A as well as in many subsequent figures in the chapter. In addition to imaging, as discussed in the Introduction, the diffraction pattern in the back focal plane may be viewed. The area of the specimen from which the diffraction pattern originates can be defined using the SAED aperture (using effectively parallel illumination) or the probe can be converged to a small area on the specimen so as to form diffraction discs (whose radius depends on the convergence angle) rather than spots. The diffraction pattern allows the degree of crystallinity as well as the exact crystallographic phase of the material to be determined as well as the incident beam direction through the crystal. See Figure 4B for a schematic diagram and also Figures 16 and 19 for an example diffraction patterns.

STEM bright field images contain all the same contrast mechanisms as CTEM bright field images, whereas STEM dark field images (particularly HAADF which relies on Rutherford scattering from the nuclei) images are relatively insensitive to structure and orientation but strongly dependent on atomic number (Z contrast), with the intensity varying as Z^{ζ} where ζ lies between 1.5 and 2. If the specimen is uniformly thick in the area of interest the HAADF intensity can be directly related to the average atomic number in the column at each pixel. Figure 4C shows an example BF and DF STEM image. If the beam is less than one atom dimension in diameter, for instance in an aberration-corrected STEM (see later), then atom column compositional resolution is therefore possible (strictly, only if we have strong channeling of the probe down the atomic columns which occurs when the sample is oriented along a low Miller index zone axis).

Analytical signals. Based on the description in the section "*Interactions between the electron beam and the specimen*", the two major techniques for chemical nanoanalysis in the

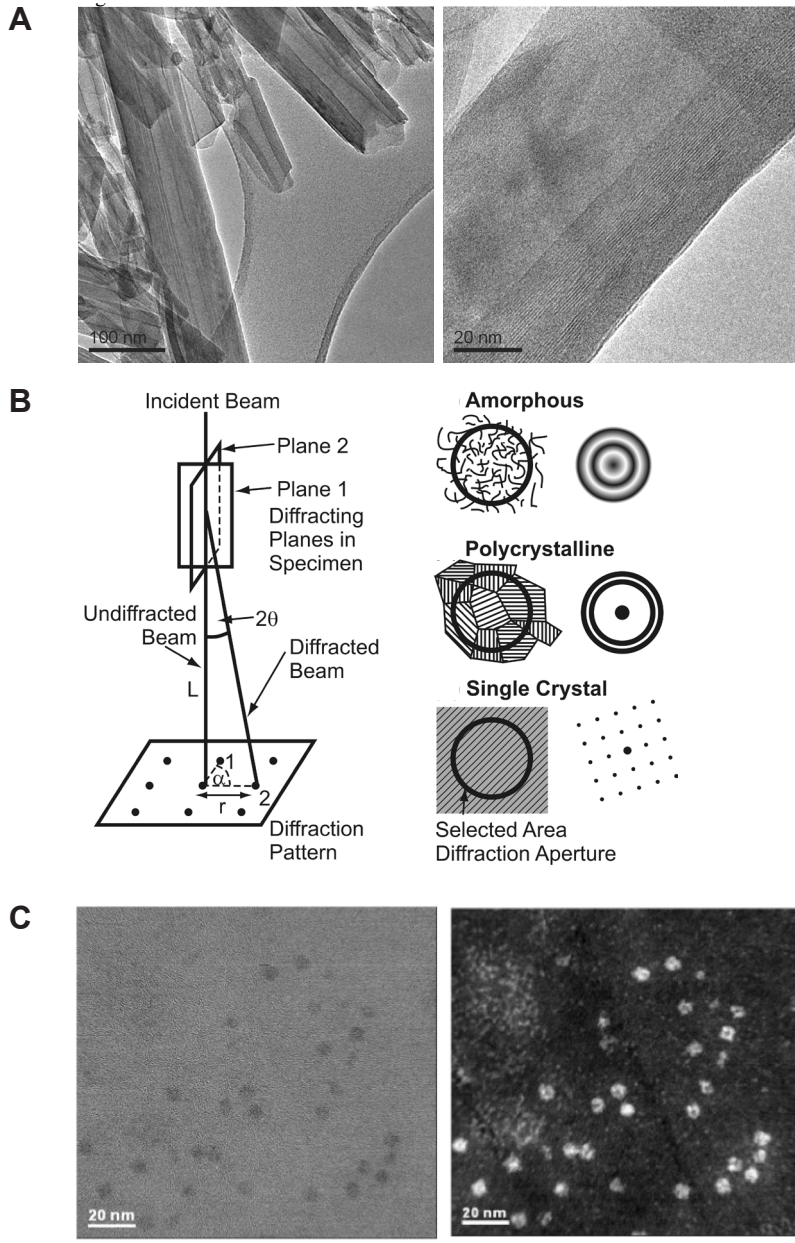

Figure 4. (A) TEM bright field image of a tubular halloysite clay mineral showing both CTEM mass thickness contrast (from the amorphous carbon support film and the halloysite tubes) and CTEM diffraction contrast from some of the halloysite tubes oriented at the Bragg angle for diffraction. At higher magnification CTEM phase contrast is evident in the (002) basal plane lattice fringes of tube walls (Brydson and Hillier, unpublished). (B) Schematic diagram of the geometry of electron diffraction in the CTEM and the form of the selected area diffraction pattern for amorphous, polycrystalline and single crystal sample regions. Examples of real diffraction patterns are shown in Figure 16 and subsequent figures. (C) Example of (*left*) a STEM BF image and (*right*) a STEM high angle annular dark field image from a cluster of iron storage proteins, ferritin molecule mineral-cores (doped ferrihydrite) cores within a tissue section (see Pan et al. 2009).

transmission electron microscope are both concerned with inelastic interactions and are based on the analysis of either the energy or wavelength of the emitted X-rays (EDX or WDX), or the direct energy losses of the incident electrons (EELS).

As shown in Figure 5, X-rays produced when the electron probe interacts with the specimen are most commonly detected from the incident surface using a low take-off angle Energy Dispersive X-ray (EDX) detector (i.e., the detector is approximately in the same plane as the sample, some 20° to the horizontal), so as to allow the detector to be brought close to the sample and also to minimize the predominantly forward-peaked Bremsstrahlung background contribution to the X-ray emission spectrum. Even though the detector is inserted to within a few mm of the sample surface, it collects only a small proportion (usually only a few percent) of the isotropically emitted X-ray signal owing to the limited solid collection angle of the detector (typically significantly less than 1 Steradian, from a total possible solid angle of 4π Steradians). Generally, the specimen is tilted towards the detector (typically through ca. 15°) so as to provide a clear X-ray trajectory between the irradiated area and the detector. The volume of the specimen that produces X-rays is controlled by the electron probe size (and hence condenser-lens currents) as well as beam broadening within the specimen that increases with (among other things) thickness and average atomic number and decreases with

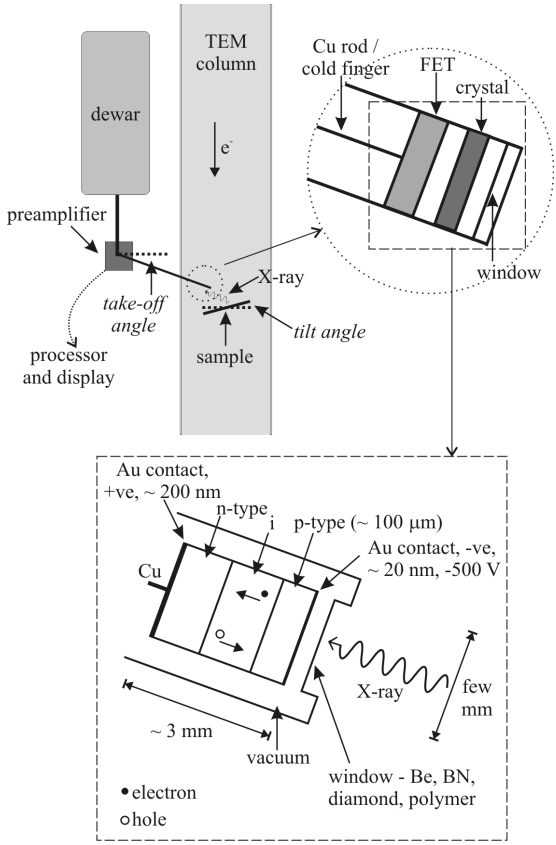

Figure 5. Energy dispersive X-ray analysis in the TEM (after Brydson 2011). Schematic diagram showing the components and location of an EDX detector in a TEM.

microscope accelerating voltage. High take-off angle X-ray detectors also exist and these do not require the specimen to be tilted towards the detector.

Below the microscope viewing screen, the self-contained EELS spectrometer (which almost always possesses a variable entrance aperture itself) and detection system collects the transmitted electron signal that is composed of both elastically and inelastically scattered electrons. In both Figures 1 and 2, α and β are known as the convergence and collection semi-angles, respectively. Note certain commercial EELS systems (particularly those initially developed for the purposes of energy-filtered imaging) employ an in-column design with the EEL spectrometer placed between the objective and projector lenses. Further details are given in the "*EDX and EELS Imaging*" section below.

As discussed in the introduction, apart from the case of energy filtered CTEM (see "*EDX and EELS Imaging*" section below), analytical information is most usually collected using a focused probe. In this respect STEMs are ideal analytical machines since they easily allow the simultaneous recording of images and X-ray emission spectra, furthermore retraction of the bright-field detector allows electrons to enter an EEL spectrometer while still simultaneously recording the HAADF image. Generally, STEMs can collect analytical EDX and EELS data in one of two ways: firstly, by scanning the beam over an area and collecting the signal from the whole scanned area and, secondly, by scanning the beam slowly and recording the analytical signal serially at each point (known as spectrum imaging). Dedicated STEMs employ extremely small probe sizes produced by cold field-emission electron sources that can provide extremely high energy resolution (EELS) and high spatial resolution (EELS and EDX) measurements.

The specimen

A specimen suitable for study by analytical TEM should be thin enough for electron transmission without significant spreading of the electron beam, yet be representative of the material about which we wish to draw conclusions. These simple requirements imply that in most cases we must prepare a thin specimen (typically less than 50 nm for high resolution studies) from a larger sample, and in all cases we must assure ourselves that the processes of preparation, mounting and examination do not change, in any uncontrolled way, the important features of the specimen. Specimen preparation is therefore an absolutely crucial aspect of analytical TEM. This is discussed in the "*Example of the practical application of EDX: clay minerals – Sample preparation*" and "*Developments in TEM specimen preparation*" sections below. However, for the vast majority of mineralogical and geological samples this usually involves cleaving or crushing a sample in an agate mortar and pestle, dispersing in a suitable inert liquid and drop-casting onto a TEM grid with a thin, usually amorphous and often holey support film. An alternative procedure, which retains the microstructural relationships in the overall specimen, involves the thinning and polishing of a bulk 3 mm disc of material cut using a drill or ultrasonic disc cutter. Course-scale thinning of the disc is usually performed mechanically using standard polishing procedures employing silicon carbide, diamond and alumina or silica abrasives of progressively decreasing roughness. Final thinning to electron transparency (ca. 100 nm) can be achieved via either: accurate and controlled mechanical polishing (tripod polishing); chemical polishing using jets of acids or alkalis or, very commonly, ion milling using a broad low energy argon ion beam. More recently the use of focused ion beam (FIB) specimen preparation techniques, although not without their specific problems associated with sample damage, has radically altered the preparation of thin TEM specimens from site-specific areas within larger samples, in particular cross sections of interfaces and surfaces (see Fig. 20 and also Giannuzzi 2004).

When analyzing the sample, the specimen should resist both contamination and damage induced by the primary electron beam. For a given incident beam energy, beam damage of the specimen is generally a function of the energy deposited within the specimen volume (known

as dose) which is dependent on the incident energy of the electron beam, the interaction cross section for the specimen, the electron fluence (i.e., the total number of electrons incident per unit area of specimen) and, in some cases, the fluence rate (usually quoted in current per unit area) can be important. In many cases, for a given set of microscope conditions, there is a "safe" fluence or fluence rate below which damage is negligible.

Beam damage of the specimen can occur by two dominant mechanisms: knock-on damage in which an atom or ion is displaced from its normal site, and ionization damage (in some contexts called radiolysis) in which electrons are perturbed leading to chemical and then possibly structural changes (Egerton et al. 2004; Williams and Carter 2009). The latter can also eventually result in specimen heating. Both types of damage are very difficult to predict or quantify with accuracy, because they depend on the bonding environment of the atoms in the specimen. In most circumstances, however, the knock-on cross section increases with primary beam energy, while the ionization cross section decreases. Thus there is a compromise to be struck for each specimen to find a beam energy that is low enough not to cause significant atomic displacement but is high enough to suppress radiolysis.

Recent developments in analytical TEM

As mentioned previously, the image resolution in CTEM is primarily determined by the imperfections or aberrations in the objective lens, while in a STEM instrument the resolution of the scanned image (as well as the analytical resolution for EDX and EELS) is determined largely by the beam diameter generated by the probe-forming lens which is also limited by aberrations. In both cases the most serious lens aberration is spherical aberration, whereby electrons travelling at differing distances from the central optic axis of the lens are focused to different positions. In recent years, technical difficulties have been overcome (principally due to increases in computing power) which has allowed both the diagnosis and correction of an increasing number (and type) of these lens aberrations (Hawkes 2008). Aberration correction could in principle be applied to any magnetic lens in any microscope. In practice there are two key areas where it is employed (in some cases in tandem) to correct spherical aberration: (i) in the condenser/illumination or probe-forming system (STEM) and (ii) in the objective or imaging lens (CTEM). With the correction of spherical aberration, the next resolution-limiting lens aberration, particularly at low accelerating voltages, is chromatic aberration whereby electrons of differing energies are focused to different positions. At the time of writing there are a number of schemes being developed and implemented for chromatic aberration correction (Leary and Brydson 2011). One of the main benefits of the correction of aberrations in STEM is in the reduction of the "beam tails" so that a fine beam positioned on a specified column of atoms does not "spill" significant electron intensity into neighboring columns. This has big implications for the STEM-based techniques of HAADF or "*Z* contrast" imaging, EELS and EDX analysis and even tomography (Brydson 2011).

Particularly with the advent of micro-electromechanical systems (MEMS) technology, it is now becoming increasingly possible to control many environmental parameters associated with the specimen while in many cases simultaneously imaging or spectroscopically analyzing a region of interest. Possible *in situ* experiments that have been demonstrated include: specimen heating or cooling, specimen straining or compression, the control of local electric or magnetic fields, measurement of local specimen conductivity, illumination of the specimen with photons, even imaging the specimen under the presence of environmental atmospheres of gas or even (flowing) liquids (see chapter by Gai (2007) in Hutchison and Kirkland (2007)).

Finally, as mentioned at the beginning of subsection "*Brief review of imaging mechanisms in CTEM and STEM,*" methodologies for three dimensional TEM image reconstructions using either tilt series tomography (see chapter by Weyland and Midgley (2007) in Hutchison and Kirkland (2007)) or single particle analysis (Pan et al. 2009) have been applied in areas

potentially akin to geology and mineralogy. In terms of analytical TEM, the basic possibilities are any signal, which monotonically increases with increasing thickness such as HAADF images and potentially EDX and EEL spectrum images or energy filtered TEM images (EFTEM) (see section below on "*EDX and EELS imaging*").

ELEMENTAL QUANTIFICATION – EDX AND EELS

EDX

As discussed previously (section "*Interactions between the electron beam and the specimen*"), following ionization of atoms in a sample by an electron beam, one possible de-excitation process is X-ray emission. The energy of the X-ray photon emitted when a single outer electron drops into the inner shell hole is given by the difference between the energies of the two excited states involved. A set of dipole selection rules determines which transitions are observed and these are labeled due to a standard notation: e.g., *K* excitation for ionization of 1*s* electrons, *L* for 2*s* (L_1) and 2*p* (actually spin orbit split into L_2 for $2p_{1/2}$, L_3 for $2p_{3/2}$) electrons etc. with corresponding subscripts (α, β, etc.) denoting the electron from the upper energy level which fills the ionized hole. Due to the well-defined nature of the various atomic energy levels, it is clear that the energies of the set of emitted X-rays will have characteristic values for each of the atomic species present in the specimen and by measuring these energies of the X-rays emitted from the sample, it is possible to determine which elements are present at the particular position of the electron probe. Figure 6 shows a typical electron-generated X-ray emission spectrum from Molybdenum oxide. The Mo K_α, K_β and L_α X-ray lines as well as the O K_α line are superimposed upon the Bremsstrahlung background. The latter X-rays are not characteristic of any particular atom but depend principally on specimen thickness. To a first approximation, peak intensities are roughly proportional to the atomic concentration of the element and, through careful measurements and comparison to elemental/mineralogical standards, EDX can detect levels of elements down to 0.1 at%. Many further example EDX spectra are given in subsequent figures.

EDX detectors collect X-rays in a near-parallel fashion and rely on the creation of electron-hole pairs in a biased doped silicon crystal (see Fig. 5); the number of electron-hole pairs and hence current is directly proportional to the energy of the incident X-ray. Fast electronics allow

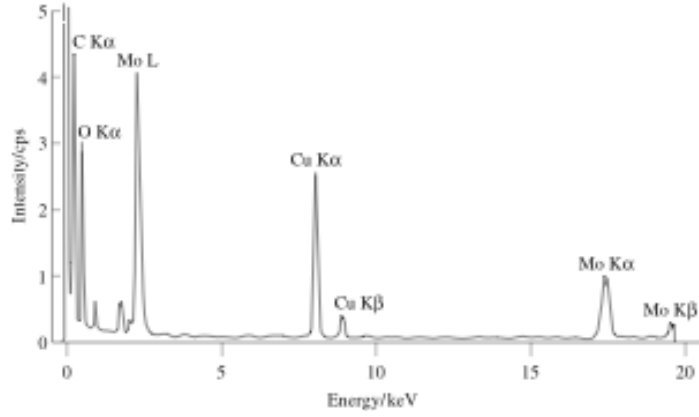

Figure 6. Schematic energy dispersive X-ray (EDX) emission spectrum from a sample of molybdenum oxide on a carbon support film. The copper K_α and K_β X-ray peaks are due to the TEM specimen holder and support grid.

separate pulses of X-rays to be discriminated and measured. EDX detectors often have some form of window (either beryllium or, for a thinner more sensitive window, a polymer) which, depending on the material and thickness, may reduce sensitivity to light elements ($Z < 11$).

New developments in EDX detectors employ silicon-drift detector (SDD) technology that have several advantages: 1) SD detectors can be designed to fit closer to the sample and subtend a greater solid collection angle so collecting more X-rays per unit time; 2) several SDD's can be linked in parallel to cover a solid collection angle approaching 1 Steradian. This requires a high level of integration of the detectors into the microscope optical design, and thus, is only available from the microscope manufacturer at the time of the publication of this chapter; 3) SDD technology can handle large amounts of incident X-rays (10^{5-6} counts/s), levels that would normally saturate the conventional Si(Li) detectors (10^{3-4} counts/s); 4) liquid nitrogen cooling is not necessary for SDD, which are Peltier cooled. This technology is still in the early stages of implementation on the TEM and promises to improve significantly elemental detection limits and also X-ray mapping capabilities.

Compared to the alternative method of detection via X-ray wavelength (Wavelength Dispersive X-ray Spectroscopy, WDX) rather than energy EDX, EDX is cheaper to implement and very fast in terms of acquisition, but it has a much poorer resolution and hence sensitivity to all elements, particularly light elements. WDX is generally confined to dedicated analytical Scanning Electron Microscopes (SEMs) known as Electron Probe Microanalyzers (EPMA), while EDX detectors may be fitted as an add-on attachment to most SEMs and TEMs.

Practical EDX acquisition and quantification. Identifying which elements are present in significant amounts from an EDX spectrum such as that shown in Figure 6 or Figure 7, is relatively routine. The positions and relative heights of the various X-ray peaks are either tabulated in references or, more commonly, are stored in a database associated with the

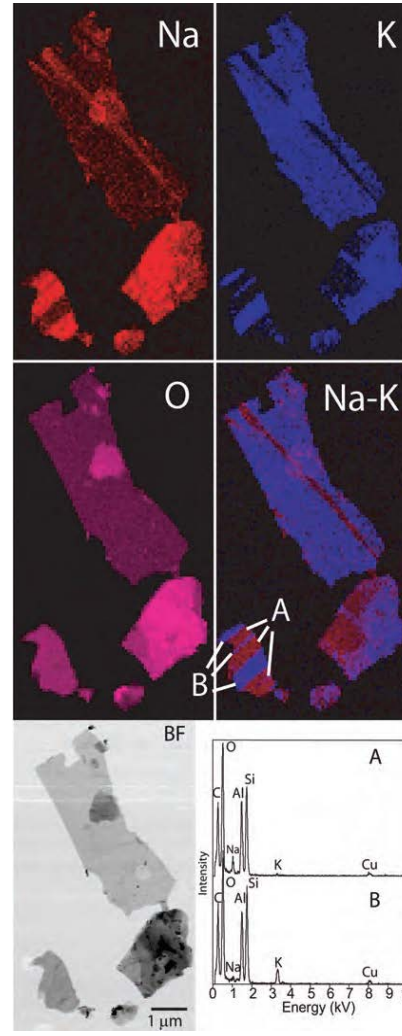

Figure 7. STEM/EDX spectrum image of mixed Na-K white micas (down c*) (from Livi et al. 2008). The Na-K X-ray image is generated by: 1) normalizing the Na and K by the O image that stands in as a proxy for thickness variations, and then 2) generating a false color (RB) image from the combined normalized maps (in electronic version Na is red and K is blue, while in print version of Na-K image Na is darker grey and K is lighter grey). The thickness variation is then effectively removed. EDX spectra integrated from areas A and B are given in the lower right. The carbon peak comes from the carbon support film and Cu is from the Cu mesh support grid.

software package of the EDX system. Working from the high-energy end of the spectrum, for internal consistency, it is necessary to confirm manually that if the *K* lines for a particular element are present, then the corresponding *L* (and possibly *M* lines) is also evident. Pre-processing of the spectrum prior to quantification involves both background subtraction and correction for escape peaks due to X-ray absorption in the surface of the detector and sum peaks due to the near simultaneous arrival (and hence detection) of two X-rays at high count rates. This may be performed using deconvolution techniques involving Fourier transformation and filtering, or alternatively both the background and escape and sum fractions may be modeled mathematically. Such facilities are an integral part of many currently available EDX software packages.

After the spectrum has been processed, the characteristic X-ray peaks are matched, using least squares methods, either to stored spectra or to computed profiles. Such a procedure can also deal with the problem of overlapping peaks. Alternatively, simple integration of areas under the peaks may be performed. Once the characteristic line intensities have been extracted the next step is to turn these into a chemical composition present in the irradiated sample volume. For quantification it is necessary to know the relevant cross sections for X-ray excitation by the accelerated electrons as well as the absorption characteristics of the window, electrode and dead layer of the X-ray detector, so as to correct the measured X-ray intensities. The most usual approach to tackling this problem is to use a proportionality factor known as a *k*-factor; this may be calculated from first principles or, more usually, it is measured experimentally. The latter approach employs a standard compound of known composition that contains the elements of interest. The basic equation for the analysis of inorganic materials is:

$$\frac{C_A}{C_B} = k_{AB}\frac{I_A}{I_B}$$

where *C* denotes the concentration in wt% and *I* denotes the characteristic X-ray peak intensity above the background, for both elements A and B. k_{AB} is the appropriate proportionality or *k*-factor, also known as a Cliff-Lorimer factor, which is independent of specimen composition and thickness but varies with accelerating voltage. Frequently, *k*-factors are measured for several element pairs that have a common element such as Si; k_{AB} is then simply given by $k_{AB} = k_{ASi}/k_{BSi}$. EDX software packages often provide a set of *k*-factors, obtained for a particular detector system at a given electron beam accelerating voltage, known as a virtual standards pack. If the specimen is very thin (a few tens of nanometers), it is possible to neglect the following phenomena: (i) the differing absorption, within the material itself, of the various characteristic X-rays generated in the specimen as they travel to the specimen exit surface en route to the detector, and (ii) fluorescence of one characteristic X-ray by another higher-energy characteristic X-ray. If however, the specimen is thicker, or for quantification of the concentration of a light element present in a heavy element matrix then, for accuracy, we have to correct for these effects, in particular absorption. The absorption correction employs an iterative procedure that initially assumes a starting composition for the specimen based on the uncorrected X-ray intensities. The absorption of different energy X-rays in this specimen en route to the detector is then accounted for using a Beer-Lambert-type expression to give a new composition that is subsequently used as input to a further absorption correction. This procedure is repeated until the change in composition falls below some preset level of required accuracy. Fluorescence by characteristic X-rays is only really significant when there are two elements of interest with similar X-ray energies and the energy of one X-ray is just above the absorption edge of another X-ray (e.g., elements close to each other in the periodic table). Fluorescence is made considerably worse by the presence of a large concentration of the fluorescing element combined with a small concentration of the fluoresced species.

With careful measurement and analysis, EDX can detect levels of elements down to 0.1 at% with an accuracy of roughly 5%. However, the absorption of low-energy X-rays becomes

a severe problem for elements of $Z < 11$ and this can make light-element quantification extremely unreliable without the use of very carefully and individually determined *k*-factors.

In terms of element detectability using analytical TEM, two important quantities are firstly, the *minimum mass fraction* (MMF), which is the smallest composition (expressed in either wt% or at%) detectable; secondly, the *minimum detectable mass* (MDM) is the minimum number of atoms detectable in the analytical volume probed. Generally for analytical transmission electron microscopy, the MMF is rather poor compared to many other analytical techniques principally due to either the low total signal detected (EDX) or the large background contribution (EELS). The ability to form small, intense electron probes means that it is possible to analyze very small total sample masses and, for a given detectable MMF, this results in a low MDM, which is one of the major benefits of analytical transmission electron microscopy; aberration correction can significantly improve this capability (see section on "*Recent developments in analytical TEM*" and Brydson 2011).

When EDX is used in the TEM, the thin nature of the TEM sample (as opposed to a bulk SEM sample) leads to much reduced broadening of the electron beam during its passage through the specimen (the so-called interaction volume) and, since EDX analysis will collect all X-rays produced isotropically within the beam-broadened volume within the specimen, the elemental analysis will possess a high spatial resolution. In practice at 100 keV, a 100 nm thick sample typically gives a beam broadening of the order of a few nanometers and by generating a small focused STEM probe, EDX spectrum imaging maps can now routinely demonstrate resolutions of 5-10 nm in thin sample areas (see Fig. 7 and also Fig. 18). However, it is important to realize that the smaller you make the probe, the more you reduce the current within the probe as electrons are "lost" in the (sometimes fixed) apertures in the column; this then means that fewer X-rays are generated lowering the spectrum signal to noise ratio (SNR). Aberration corrected STEMs, can achieve ultrafine electron probes with more current and very high (even atomic column) resolution EDX maps have been demonstrated, most probably at the risk of increased beam damage and hydrocarbon contamination (Brydson 2011). However, such high spatial resolution mapping requires the use of high solid angle, high throughput EDX SDDs which can significantly increase count rates both collected and processed by the detector. This has significantly enhanced EDX spectrum imaging capabilities both in terms of acquisition times and spatial resolution.

Below we outline the major issues associated with the practical application of TEM/EDX in mineralogical research.

Example of the practical application of EDX: clay minerals

The development of TEM techniques has been very beneficial to the study of clay minerals owing to their grain size (<1 μm) being generally below the resolution of electron microprobe (EPMA) techniques. Analytical TEM using light element detectors has become a standard tool for "nanopetrologists" interested in the compositions of individual crystals of clay minerals (see Merriman and Peacor 1999 for description of EDX applications to low-grade metamorphism). The purpose of this section is not to summarize the extensive work of analytical TEM applications to clay minerals, but to outline some protocols that should be adhered to when attempting to obtain quantitative data on nanoparticles. Potential pitfalls become apparent when the analytical volumes decrease in our attempts to obtain greater resolution and detail of intergrowths and mineral boundaries—especially in beam sensitive minerals.

Sample preparation. Several factors can influence elemental analysis during sample preparation. These include elements introduced during the preparation or alteration of sample composition during the process of thinning the sample.

- *Choice of TEM support grid metal.* Copper, which is a common choice for the grid metal, has an L_α X-ray line that interferes with the analysis of sodium. The tantalum and tungsten *M* lines overlap with silicon and may complicate background subtraction in that keV range. Molybdenum will overlap with sulfur, and steel will complicate analysis of iron, nickel and chromium. It is important to understand how your support grid metal will influence your analysis. Choose a metal to meet your analytical needs. If need be, manufacture your own using hole punches and drills.
- *Ar ion milling.* Argon ion milling can cause smearing of elements across mineral interfaces (Schmidt et al. 1999). Ion milling can also cause loss of volatile elements through heating of the specimen during milling. To minimize these effects, liquid nitrogen cooled milling is recommended. However, make sure the sample is not the coldest component in the mill or else contaminants will condense on the sample. Oxidation or reduction can take place in the vacuum of the ion mill. An example of this is the reduction of pyrite to nanocrystalline pyrrhotite (unpublished data).

  Ion milling creates an amorphous layer on the top and bottom of mineral samples. The proportion of amorphous material in analytical volumes will increase as the thickness of the foil decreases. Low-energy polishing may remove much of the amorphous layers and this is facilitated by new ion mills with ion guns capable of operating at very low energies.
- *Focused Ion Beam (FIB) cross sectioning.* During the production of FIB sections, implantation of gallium will occur. The Ga L_α interferes with Na K_α analysis, so a good final polish at low keV and low beam current is necessary to remove the implanted gallium and amorphous material that may have been added during foil preparation. Good preparation of FIB sections will produce uniformly thin foils. It is then necessary to determine if the foil thickness will satisfy the Cliff-Lorimer thin-film criteria.
- *Crushed grain mounts on TEM support films.* These mounts are extremely useful in cases where spatial relationships between grains are not needed. Sample preparation times are short (5 min) and there is little chance of sample contamination if care is taken. A few issues are important to pay attention to though. Use clean thin holey- or lacey-carbon support films and deionized-distilled water (or freshly-opened 200 proof alcohol) as the suspension fluid. Silicon, sulfur, sodium, chlorine and calcium can be found as contaminants introduced during the manufacturing process or from suspension solution. Check the presence of these elements by analyzing areas of the support film close to the grain of interest. The use of deionized-distilled water can sometimes leach sodium and potassium from minerals such as albite and especially Na-rich sheet silicates. With these minerals, use tap water as the suspension fluid and check for sodium, chlorine, and calcium contamination on the support film.
- *Tripod polishing.* Tripod polishing is good for large mineral grains and their interfaces, but not fine-grained or loosely aggregated particles. Crystal bond adhesive is typically used to fix samples to the pedestal and this adhesive makes it difficult to thin small particles without loosening them.

Calibration of EDX detector. Although instrument manufacturers sell detectors with estimated efficiency parameters, it is highly recommended that empirical *k*-factors be determined for each detector. It is best to determine these *k*-factors for specific conditions (i.e., incident keV, pulse processing rate, peak integration width) using known mineral standards.

Sample geometry. Make sure the sample is tilted towards the detector during analysis, but not too high a tilt since this will increase the fluorescence of the support grid metal (e.g.,

Cu) by bremsstrahlung radiation. Make sure there is a clear path for X-rays to enter the EDX collimator. If not, this can cause subtle absorption of light relative to heavy X-rays. It is important to know, for a given image magnification, the direction in which the EDX detector lies. This can be accomplished by partially retracting the sample holder carefully and determining the tilt axis and tip direction of the holder. This should be determined for all magnifications since the image rotation often changes with magnification. When analyzing grain mounts, large particles and even support grid bars can occlude X-ray detection, therefore, take care to determine if you are on the detector side of the particle or grid for unobstructed X-ray collection.

Sample thickness. Quantitative AEM analyses require that the Cliff-Lorimer thin-film criteria (C-LTFC) be satisfied for all elements analyzed. This criterion has been stated as the thickness of the foil where absorption of any element is less than 3% (Williams and Carter 2009). A more practical criterion would be the thickness that the ratio of any two elements changes by less than 3%. This can be calculated or determined empirically through analyses along the foil wedge. Be aware that the thinnest C-LTFC will be for samples containing both light and heavy X-rays (e.g., sodium and iron). One tip to determine if there is absorption of low-energy X-rays, is to observe the slope of the background below 1 kV. This should continue to rise up to the cutoff of the lower-level discriminator setting value, or in some systems, the zero-strobe peak. Absorption corrections can be made in most commercial software packages if the thickness is known, although this is not trivial to measure.

An alternative method for correcting for samples thicker than the C-LTFC was proposed by van Cappellen and Doukhan (1994). This method uses the calculated cation to oxygen ratio to determine if electroneutrality is satisfied (i.e., if proper oxygen stoichiometry is met). An absorption correction is applied to balance cation and oxygen atom proportions. This method is not applicable if the valences of elements such as iron and manganese are not known.

The generation of STEM/EDX images present an interesting problem that the variation of sample thickness influences the intensity of an X-ray signal independently of compositional variation. This can lead to false conclusions of concentration variance where there is none or hide variations that exist. Figure 7 presents a case where the relative compositional constancy of an element (in this case oxygen) can be used to ratio with other elements and generate first order thickness-normalized images. Livi et al. (2008) investigated the occurrence of K- and Na-rich intergrowths in very low-grade prograde metamorphic white micas. They obtained low-dose STEM/EDX images of white mica flakes with the basal normal parallel to the electron beam. Although the flakes were relatively flat, some thickness variation existed which degraded the image quality and increased the difficulty of interpretation of intensity variations. They took advantage of the fact that O content was nearly identical in both the paragonite (Na) and muscovite (K) rich regions and normalized the Na and K X-ray intensity maps to the O map, in proxy for thickness. The O map clearly indicates where thickness changes are, and the improvement in image quality can been seen in the combined red (Na) and blue (K) image. By this processing, the unusual boundaries of the Na-K intergrowths in the lower right crystal can be discerned.

This type of "quick" thickness correction will break down when the thickness variation of the sample is more extreme. The best solution for thickness variation is to perform a full quantitative reduction of each spectrum at every pixel. This, first of all, is best done when the data is collected as a "spectrum" image that stores a full spectrum at every pixel. Then there has to be an estimate of the thickness at every pixel. For minerals with known stoichiometry, the method of van Cappellen and Doukhan (1994) could be used and the resultant image is a fully quantitative map. In some cases, the continuum background may be used as a reference image if sufficient counts are generated. Alternatively, the simultaneous EELS acquisition of the zero-loss and plasmon peaks could be used to estimate the thickness (Egerton 2011). In this method,

there has to be a balance between the need for high beam fluxes for good EDX statistics and low fluxes to ensure that the EELS detector is not damaged or saturated. In all of these methods, there is an increase in the variation of the element intensity due to the summation of errors in each map. As in any analytical method, it is a good idea to perform an error analysis to determine the initial count rate needed to distinguish the desired compositional contrast.

Besides the Cliff-Lorimer method, recently a new EDX quantitative method called the ζ (zeta)-factor approach has been developed which incorporates both the absorption correction and also the fluorescence correction (Williams and Carter 2009) and, in addition to estimating composition, provides a simultaneous determination of the specimen thickness. ζ-factors can be recorded from pure element standard thin films provided the beam current and hence the electron fluence during EDX acquisition is known.

Microscope operating conditions. The microscope conditions focus on establishing an electron fluence (electrons/nm^2) during which there is statistically no loss of elements due to volatilization or diffusion. It does not matter if the structure becomes altered or amorphous, as long as the chemical composition remains constant. However, structural alteration is often accompanied by compositional changes—especially when considering oxidation changes of transition elements (Livi et al. 2012). Fluence is a function of four parameters: 1) Beam current—which is set by the first condenser lens and the emission current (gun bias) in a conventional source TEM, and additionally by the gun lens setting and extraction voltage in a FEG; 2) Beam diameter—which is set by the second condenser lens or the particular lens settings for a scanning beam (microprobe or nanoprobe modes); 3) Analysis time—which should include the time to set up the acquisition (beam placement and computer setup and the scan rate during STEM analysis; 4) Microscope accelerating voltage (strictly this affects dose).

Time-series analyses should be used to determine the highest fluence possible to maximize precision and spatial resolution before loss of any element occurs. Fluence in the STEM is often varied by the scan rate of the beam. However, areas scans in STEM are often achieved by not only scanning quickly over the area displayed on the computer or CRT, but also include two dwell positions outside the view area. In order to reduce distortions in scanned images, two reference positions are established: one just outside the initial corner of the image and one at the starting point of each scanned line. X-rays generated from these reference points are included in the acquired spectrum and are disproportionally counted. Since they are analyzed at greater fluences than the viewed area, they may experience greater beam damage and bias the integrated area analysis.

Fluence in conventional TEM mode is varied by beam diameter and shape. In cases where analyses of linear features are required (a thin edge, elongated precipitate, or an interface), the condenser lens stigmation can be set to elongate the beam parallel to that feature. This lowers the fluence and maintains spatial resolution in one direction without loss of X-ray production. An alternative could be to move the beam along a feature of interest during X-ray collection.

A special case for clay minerals occurs due to their thin sheet morphology in grain mounts. This produces thin areas for analysis, but elements like sodium and potassium can diffuse during condensed beam analysis. To mitigate this, it is recommended to spread the beam (in CTEM mode) such that it extends to just larger than the sheet. Sodium and potassium will diffuse within the grain, but there will be less volatilization.

Adhering to these protocols will help ensure the acquisition of high-quality EDX analyses. The evaluation of the accuracy of analyses may sometimes be achieved through calculation of mineral formulae and determination if site occupancies are reasonable. However, the possibility of mixed valence elements, vacancies, missing species from the analyses (e.g., H_2O, CO_2, lithium, beryllium and boron) and non-stoichiometry render mineral formulae inaccurate.

EELS

As discussed previously, Electron Energy-Loss Spectroscopy (EELS) in a S/TEM involves analysis of the inelastic scattering suffered by the transmitted electron beam (Brydson 2001; Egerton 2011). Measurement of the transmitted electron-energy distribution is achieved by dispersing the electrons according to their kinetic energy (and hence energy loss during passage through the sample) using an electron spectrometer most usually based on a magnetic field normal to the electron beam, as shown in Figure 1. The electron energy loss spectrum is almost exclusively recorded in parallel using a scintillator optically coupled to either a one- or two-dimensional photodiode array detection system. This produces a spectrum consisting of typically 1000 channels or pixels. The dispersion of the spectrometer may be varied so that different spectral energy ranges can be made incident on the detector, typically varying from about 100 eV to up to 2000 eV wide. In practice owing to the large dynamic range in the EEL spectrum (up to 10^8), a whole EEL spectrum is nearly always recorded in separate energy portions by applying an offset voltage to a drift tube through which the electrons travel during their passage through the dispersing magnetic field. This shifts the spectrum across the detector and each individual spectral section needs to be energy calibrated using either an accurate drift tube voltage applied to shift a known feature such as the intense zero loss peak, or the known energy of a reference feature within a particular spectral region (such as the carbon K-edge onset).

The various inelastic scattering processes outlined above each provides valuable information on the sample area that is irradiated by the electron probe. The technique can provide high-resolution elemental analysis and mapping as well as a means of determining the local electronic structure, in crude terms the local chemical bonding. These are discussed in more detail in subsequent sections.

Practical EELS acquisition and general features in the EEL spectrum. Practically, there are two main ways to operate the microscope when recording EEL spectra:

1. Operate in STEM mode with the electron probe focused onto the specimen with a semi-angle of convergence (α) typically in the range 2-15 mrad (see Fig. 2). The area irradiated by the probe effectively determines the spatial resolution for analysis. The highly forward peaked EELS signal is collected over a semi-angle (β) defined by the spectrometer entrance aperture (SEA) and the camera length (effectively the magnification of the diffraction pattern) or alternatively, in a dedicated STEM, a post-specimen collector aperture may be employed to define β. In general, for efficient signal collection, the collection semi-angle should be chosen so as to be significantly larger than the convergence semi-angle.
2. Operate in TEM diffraction mode with a near parallel beam and the selected area diffraction (SAED) aperture effectively defining the area of analysis (typically ranging from 150 nm to a few microns in diameter); in this mode, both the camera length of the diffraction pattern and the SEA define the collection semi-angle (β). Here the collection semi-angle should be chosen so as to efficiently collect as many inelastically scattered electrons as possible so as to give a good signal to noise ratio while not inducing a large background contribution to the spectrum; typically this would be a value in the range 5-15 mrad at 200 keV incident beam energy.

Additionally please note that in energy filtered TEM (see later) the microscope is operated in TEM image mode.

As mentioned above, spectra are most often recorded using a scintillator and a two-dimensional array of a CCD, identical to that used for the digital recording of TEM images. These systems rely on the measurable discharge (over a certain integration time) of a large array

of self-scanning, cooled silicon diodes by photons created by the direct electron irradiation of a suitable scintillator. This spectral signal is superimposed on that due to thermal leakage currents as well as inherent electronic noise from each individual diode and together these are known as dark current that can be subtracted from the measured spectrum; gain variations and cross-talk between individual diode elements can also be measured and corrected for following spectrum acquisition.

Once recorded and pre-processed, the various energy losses observed in a typical EEL spectrum are shown schematically in Figure 8A, which displays the scattered electron intensity as a function of the decrease in kinetic energy (the energy loss, *E*) of the transmitted fast electrons. This represents the response of the electrons in the solid to the electromagnetic disturbance introduced by the incident electrons. As noted previously, the intensity at 2000 eV energy loss is typically eight orders of magnitude less than that at the zero-loss peak and therefore, for clarity, in Figure 8A a gain change has been inserted in the linear intensity scale at 150 eV. In a specimen of thickness less than the mean free path for inelastic scattering (roughly 100 nm at 100 keV), by far the most intense feature in the spectrum is the zero-loss

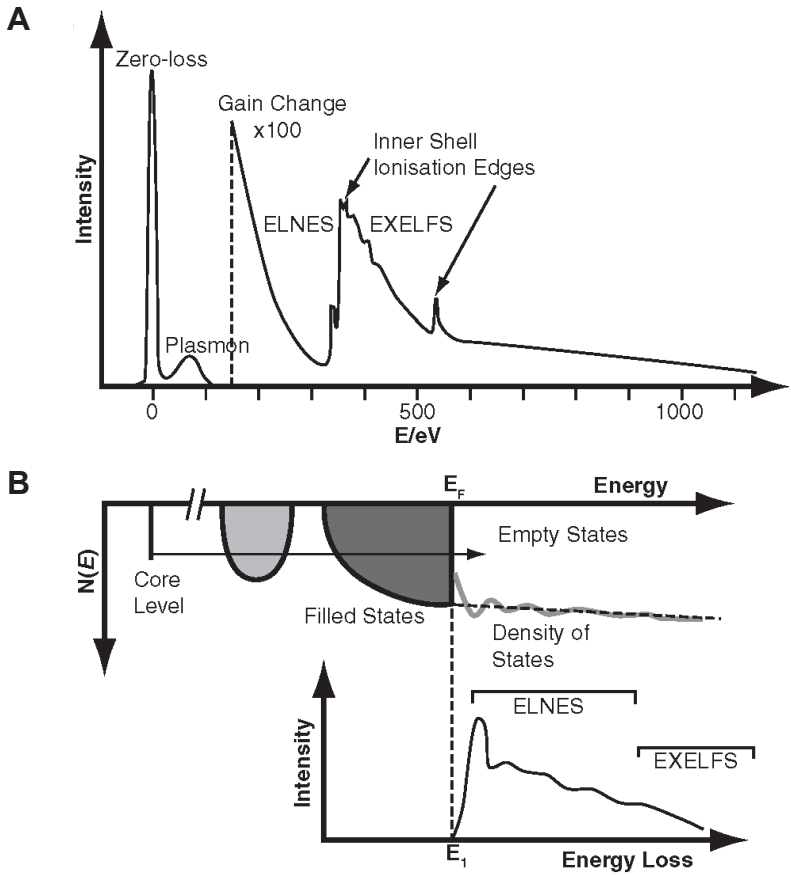

Figure 8. Schematic diagram of (A) a general EEL spectrum (with a linear intensity scale and a gain change at ca. 150 eV) showing all of the observable features and (B) an enlarged version the (background-subtracted) ELNES intensity indicating how it reflects transitions from atomic core levels to the unoccupied DOS above the Fermi level (after Brydson 2001, 2011).

peak at 0 eV energy loss that contains all the elastically and quasi-elastically (i.e., vibrational- or phonon-) scattered electron components. Neglecting the effect of the spectrometer and detection system, the Full Width Half-Maximum (FHWM) of the zero-loss peak is usually limited by the energy spread inherent in the electron source. In a TEM, the energy spread will generally lie between 0.3-3 eV, depending on the type of emitter (cold field emission < Schottky < LaB_6 thermionic < tungsten thermionic emitter), and this parameter often determines the overall spectral energy resolution. In recent years, the use of electron monochromators has improved achievable spectral energy resolutions to 0.1 eV or less, generally at the expense of probe current.

The low-loss region of the EEL spectrum, extending from 0 to about 50 eV, corresponds to the excitation of electrons in the outermost atomic orbitals that are delocalized in a solid due to interatomic bonding and may extend over several atomic sites. This region therefore reflects the solid-state character of the sample. The smallest energy losses (10-100 meV) arise from phonon excitation, but these are usually subsumed in the zero-loss peak. The dominant feature in the low-loss spectrum arises from collective, resonant plasmon oscillations of the valence electrons. The energy of the plasmon peak is governed by the density of the valence electrons, and its width by the rate of decay of this resonant mode. In a thicker specimen (> 100 nm) there are additional (harmonic) peaks at multiples of the plasmon energy, corresponding to the excitation of more than one plasmon; the intensities of these multiple Plasmon peaks follow a Poisson statistical distribution. A further feature in the low-loss spectra of insulators are peaks, known as interband transitions, which correspond to the excitation of single valence electrons to low-energy unoccupied electronic states above the Fermi level. Besides more detailed analysis, the low-loss region can be used to determine the relative (or absolute) specimen thickness and to correct for the effects of plural inelastic scattering when performing quantitative microanalysis on thicker specimens (see ahead).

Correspondingly, the high-loss region of the EEL spectrum extends from about 50 eV to several thousand electron volts and corresponds to the excitation of electrons from localized orbitals on a single atomic site to extended, unoccupied electron energy levels just above the Fermi level of the material (Fig. 8B). This region therefore more reflects the atomic character of the specimen. As the energy loss progressively increases, this region exhibits steps or edges superimposed on the monotonically decreasing background intensity that usually follows an inverse power law, $I = AE^{-r}$. These edges correspond to excitation of inner-shell electrons and are therefore known as ionization edges. The various EELS ionization edges are classified using the standard spectroscopic notation similar to that employed for labeling X-ray emission peaks; e.g., K excitation for ionization of $1s$ electrons, L_1 for $2s$, L_2 for $2p_{1/2}$, L_3 for $2p_{3/2}$ and M_1 for $3s$, etc. The subscript, in for example $2p_{1/2}$, refers to the total angular momentum quantum number, j, of the electron that is equal to the orbital angular momentum, l, plus the spin quantum number, s, which can couple either positively or negatively.

Practical EELS quantification. Since the energy of the ionization edge threshold is determined by the binding energy of the particular electron subshell within an atom—a characteristic value, the atomic type may be easily identified with reference to a tabulated database. The signal under the ionization edge extends beyond the threshold, since the amount of kinetic energy given to the excited electron is not fixed. The intensity or area under the edge is proportional to the number of atoms present, scaled by the cross section for the particular ionization process, and hence this allows the technique to be used for *quantitative analysis*. EELS is particularly sensitive to the detection and quantification of light elements ($Z < 11$) as well as transition metals and rare earths.

Problems can arise if the sample thickness is greater than the mean free path for inelastic scattering, in this case plural inelastic scattering (i.e., a few such inelastic scattering events) will occur. This will significantly increase the low loss Plasmon intensities, leading to an increase in

the background contribution making it difficult to identify the presence of edges in a spectrum. A further effect of plural inelastic scattering is the transfer of intensity away from the edge threshold towards higher energy losses due to the increase of double scattering events involving a plasmon excitation followed by an ionization event or vice versa. It is possible to remove this plural inelastic scattering contribution (at the expense of some added noise) from either the whole EEL spectrum or a particular spectral region by Fourier transform deconvolution techniques. Two techniques are routinely employed, one, known as the Fourier-log method, requires the whole spectrum over the whole dynamic range as input data. This large signal dynamic range can be a problem with data recorded in parallel. The second, known as the Fourier-ratio method, requires a spectrum containing the feature of interest (i.e., an ionization edge) that has had the preceding spectral background removed. A second spectrum containing the low-loss region from the same specimen area is then used to deconvolute the ionization edge spectrum.

After some initial data processing, such as dark-current subtraction, gain correction (which are both a function of the response of the detection system outlined previously) and also possibly deconvolution to remove the effects of multiple inelastic scattering in thicker specimen regions, in order to quantify the elemental analysis it is necessary to measure the intensities under the various edges. This is achieved by fitting a background (in many cases a power law, $I = AE^{-r}$, where A is a constant, r the inverse power law exponent and E the energy loss) to the spectrum immediately before the edge. This is then subtracted (Fig. 9A) and the intensity is measured in an energy window, Δ, which begins at the edge threshold and usually extends some 50 to 100 eV above the edge. The next step is to compute the inelastic partial cross section, σ, for the particular inner-shell scattering event under the appropriate experimental conditions, i.e., $\sigma(\alpha, \beta, \Delta, E_o)$, where the bracketed terms simply represent the variables on which the partial cross section depends. This partial cross section is calculated for the case of a free atom using simple hydrogenic or Hartree–Fock–Slater wavefunctions and is generally an integral part of the analysis software package. The measured edge intensity is normalized (i.e., divided) by the partial cross section so that either different edge intensities can be compared (Fig. 9B,C), or the intensity can be directly interpreted in terms of an atomic concentration within the specimen volume irradiated by the electron probe. For the latter case, the measured edge intensity is divided by both the partial cross section and the combined zero loss and low loss intensity measured over the same energy window, Δ; the result is usually expressed in terms of an areal density in atoms/nm^2 multiplied by the specimen thickness (Pan et al. 2008, 2009).

An example of relative EELS elemental quantification on minerals is provided in Figure 18 and also Engel et al. (1988). Apart from the case of light elements as well as many of the transition metal and rare earth elements, detection limits for EELS are generally worse than those for EDX and typically lie between 0.1 and 1 at%. This is principally due to the limited spectral range of the technique relative to EDX as well as the steep and intense background signal upon which the ionization signal lies. Meanwhile, analytical accuracies in elemental quantification usually lie in the range 5-10%.

EEL SPECTROMETRY

EEL low-loss spectroscopy

The low-loss region of the EEL spectrum provides a high signal intensity, which is often recorded as one spectral region containing the zero loss peak, or, alternatively, the zero loss is displaced off the detector to increase the SNR. The low loss is dominated by the bulk plasmon excitation, which may be thought of as a resonant collective oscillation of the valence electron gas of the solid (as pictured in the Drude-Lorentz model for metals) stimulated by the fast incident electron. Employing the free-electron model of solids, which works surprisingly well for a range of elements and compounds including minerals, the bulk plasmon energy, E_p, is

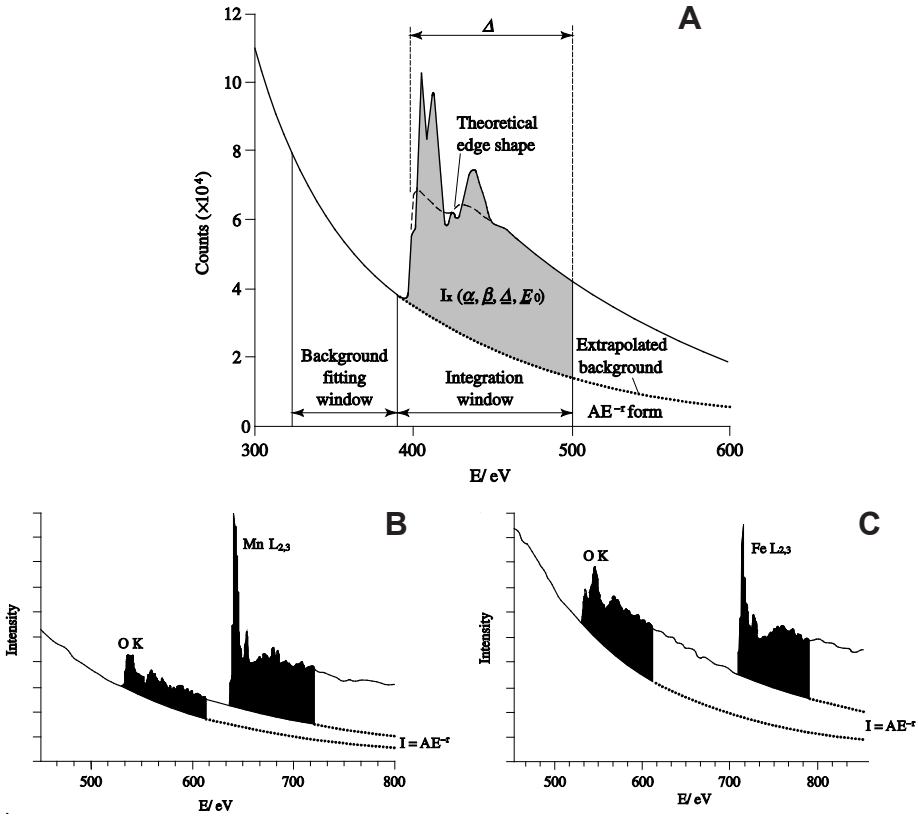

Figure 9. Diagram showing the details of EELS quantification procedures (after Brydson 2001). (A) The nitrogen *K*-edge from thin sample of boron nitride with a power law background fitted in a window prior to the edge and extrapolated over a window of width, Δ, under the edge. Also shown is a theoretical N *K*-edge cross-section calculated using the Hydrogenic model after convolution with the low loss region of the spectrum to simulate the effects of multiple inelastic scattering. EEL spectra of (B) MnO and (C) α-Fe_2O_3. In both cases fitted power law ($I = AE^{-r}$) backgrounds are indicated by dotted lines. The shaded areas extend for an energy window, Δ = 80 eV, above each edge threshold and are used to quantify the elemental analysis as described in the text.

predicted to be proportional to the square root of the valence electron density. Free-electron metals, such as aluminum, show very sharp plasmons, while in minerals, which are generally insulators and semiconductors, the plasmon peak is considerably broader since the valence electrons are damped by scattering with the ion-core lattice. The sensitivity of the plasmon peak position to changes in valence-electron density, potentially allows any chemical or structural rearrangements in, for example, different microstructural phases or changes in the degree of ordering to be detected as shifts in this plasmon energy. For example, the plasmon energy of graphitizing carbons (see Fig. 10A) correlates well to the long-range structural order (graphitic character and sp^2 carbon content) and density of the specimens, which in turn is a function of their thermal history (Daniels et al. 2007). See Figure 13 for a selection of low loss spectra.

In addition to plasmon oscillations, the low-loss region may also exhibit interband transitions, i.e., single electron transitions from the valence band to unoccupied states in the conduction band, which appear as peaks superimposed on the main plasmon peak (see Fig. 10A). If a mineral is an insulator and possesses a bandgap there should be no interband

transitions below the bandgap energy and thus, once the zero loss peak has been modeled, extrapolated and removed from the rest of the spectrum, it is possible to extract the bandgap associated with an initial rise in intensity in the low-loss region, as seen in Figure 10B-D for the case of diamond.

A full analysis of the low-loss region is based upon the extraction of the dielectric function, ε, of the material. This is a complex quantity, which represents the response of the entire solid to the disturbance created by the incident electron. The same response function describes the interaction of photons with a solid and this means that energy-loss data may be correlated with the results of optical measurements in the visible and UV regions of the electromagnetic spectrum, including quantities such as refractive index, absorption and reflection coefficients.

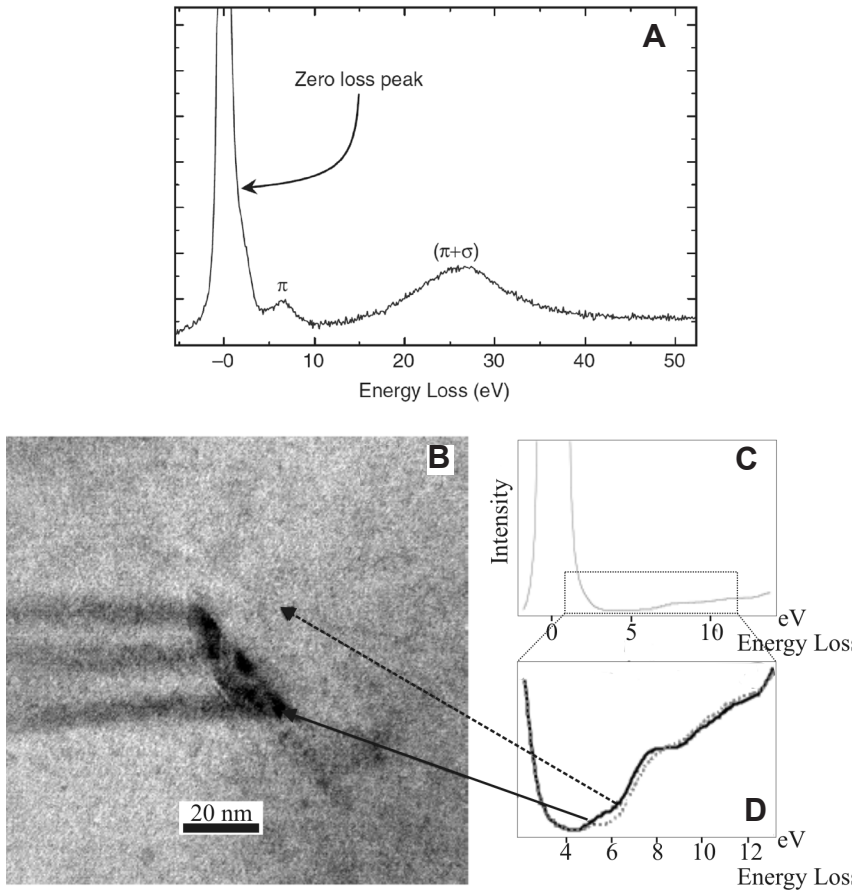

Figure 10. (A) The EELS low loss region of a partially graphitic carbon. The feature at 6.5 eV arises from an interband transition between the π bonding and π* antibonding orbitals. The bulk valence plasmon (at ca. 26 eV) arises from a collective oscillation of the valence electrons. (B) STEM BF image of a stacking fault arrangement in CVD single crystalline diamond comprising of primary and secondary faults. (C) EEL spectra taken at locations of the arrows, i.e., in the perfect crystal (grey) and near the stacking fault (black). The difference can be seen more clearly in the expanded view in (D) where enhancement in the joint density of states in the vicinity of the partial dislocations bounding the stacking fault occurs due to energy states below the conduction band edge (~5.5 eV) and due to contribution of sp^2 bonding (~7 eV). See Bangert et al. (2005) for further details.

EELS core-loss fine structure

For solids, the change in the cross section for inner-shell ionization as a function of energy loss (known as the energy differential cross section) and therefore the detailed shape of the ionization edge is not in fact solely that due to an isolated atom (as is assumed in the basic EELS quantification process). In reality it is proportional to a site- and symmetry-projection of the unoccupied density of electron energy states (DOS). Since the exact form of both the occupied and unoccupied DOS will be appreciably modified by the presence of bonding between atoms in the solid, this will therefore be reflected in the detailed ionization edge fine structure known as electron loss near-edge structure (ELNES) (Ahn 2004).

In many cases it is found that, for a particular elemental ionization edge, the observed ELNES exhibits a structure that, principally, is specific to the arrangement, i.e., the number of atoms and their geometry, as well as the type of atoms solely within the first coordination shell (Brydson et al. 1988, 1989). This occurs whenever the local DOS of the solid is dominated by atomic interactions within a molecular unit and is particularly true in many non-metallic systems such as semiconducting or insulating minerals where we can often envisage the energy band structure as arising from the broadened molecular orbital levels of a giant molecule. If this is the case, we then have a means of qualitatively determining nearest-neighbor coordinations using characteristic ELNES shapes known as coordination fingerprints. This is similar to the use of near-edge structure (XANES or NEXAFS) in the analogous (though less spatially resolved) technique of X-ray absorption spectroscopy (XAS) (de Groot and Kotani 2008, see also Fig. 16). A wide range of cations (e.g., aluminum, silicon, magnesium, various transition metals, etc.) in different coordinations and anion units (e.g., borate, boride, carbonate, carbide, sulfate, sulfide, nitrate, nitride, etc.) in inorganic solids show this behavior that can be of great use in phase identification and local structure determination (see Fig. 11A; and also see review by Drummond-Brydson et al. (2004) in Ahn (2004)).

For certain edges, as well as for certain compounds, the concept of a local coordination fingerprint breaks down. In these cases, the unoccupied DOS cannot be simply described on such a local level and ELNES features are found to depend critically on the arrangement of the atoms in outer-lying coordination shells allowing medium-range structure determination. This opens up possibilities for the differentiation between different structural polymorphs, the characterization of the structure of localized defects, intergrowths or interfaces as well as the accurate determination of lattice parameters, vacancy concentrations and substitutional site occupancies in complex structures (Scott et al. 2001).

Using density functional band structure calculations (or their equivalents) it is possible to model the unoccupied DOS and compare this directly with measured ELNES (see Fig. 11). The calculated electron energy bands need to be integrated into a density of electronic states which need to be resolved into a site projection in the unit cell for the atom undergoing ionization and also an angular momentum symmetry projection for the exact final states which are accessed by the excited electron under the dipole selection rule (which states that the change in orbital angular momentum, Δl, between the initial and final states of the transition is ± 1). Currently a number of different approaches are commonly used, among which are: WIEN2K (*http://www.wien2k.at*; Schwarz et al. 2002); CaSTEP (*http://www.castep.org/*; Clark et al. 2005); FEFF (*http://leonardo.phys.washington.edu/feff/*; Ankudinov et al. 1998), all of which now have specific modules to enable output of EELS spectra. Wien2k is what is known as an all electron code and expands the electron wavefunctions as plane waves, whereas CaSTEP is a pseudopotential code, approximating tightly bound inner core levels as part of the potential term so allowing more complex systems to be handled. Both codes perform calculations in reciprocal space and thus require a periodic system (i.e., a unit cell). Meanwhile FEFF calculates electronic states by considering multiple (elastic) scattering (MS)

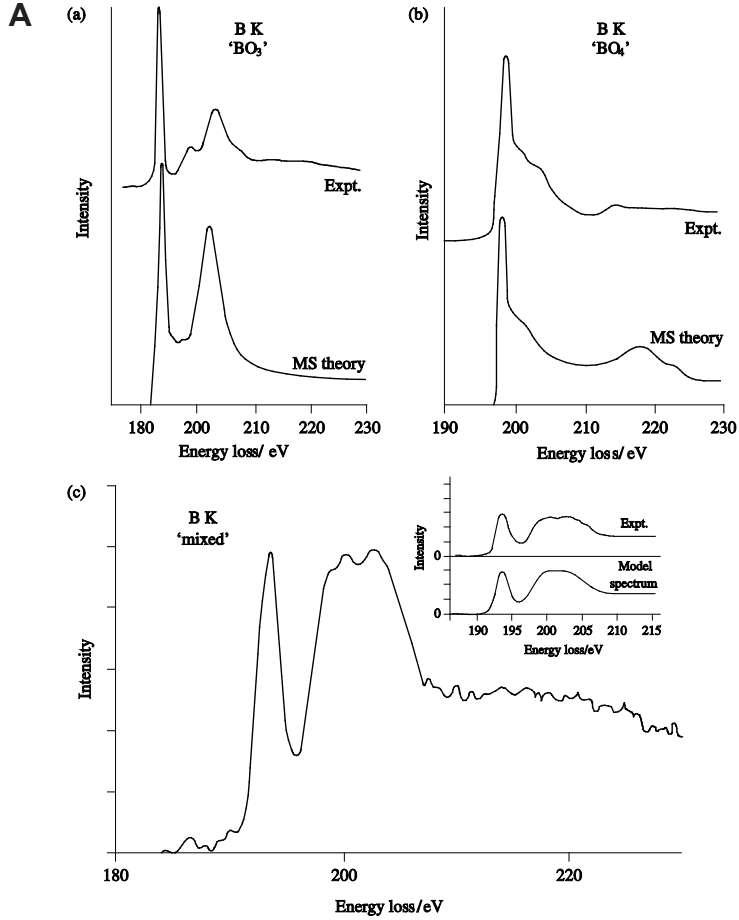

Figure 11. (A) An example of ELNES coordination fingerprinting after Sauer et al. (1993). A comparison of the B K-ELNES from: (a) the mineral vonsenite containing trigonal planar BO_3 groups; (b) the mineral rhodizite containing tetrahedral BO_4 groups and (c) a mixed coordination boron-doped Fe,Cr oxide. In (a) and (b) the experiment (*Expt.*) is compared to the results of single shell MS calculations (*MS Theory*) indicating the existence of trigonal and tetrahedral B K-ELNES coordination fingerprints. Inset in (c), the experimental data has been modeled using a linear combination the B K-coordination fingerprints in the ratio 3:1 (trigonal: tetrahedral). ***figure continued on next page***

of the excited electron with a real space cluster, which more easily allows the study of non-periodic structures.

As well as determining coordinations, ELNES can be used for the spatially resolved determination of the formal valency or oxidation state of elements in minerals (see Fig. 11B). The valence state of the atom undergoing excitation influences the ELNES in two distinct ways. Firstly, changes in the effective charge on an atom lead to shifts in the binding energies of the various electronic energy levels (both the initial core level and the final state) that often manifest as an overall chemical shift of the edge onset. Secondly, the valence of the excited atom can affect the intensity distribution in the ELNES. This predominantly occurs in edges that exhibit considerable overlap between the initial and final states and hence a strong interaction between the core hole and the excited electron leading to the presence of

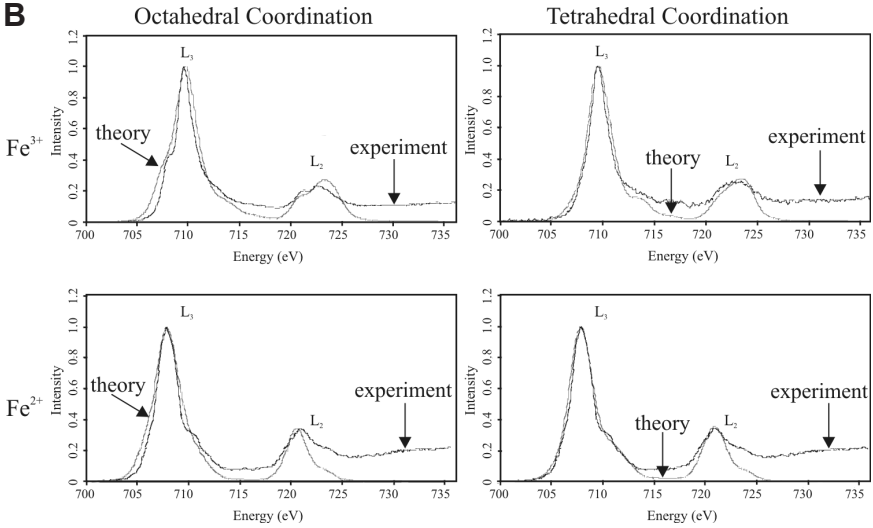

Figure 11. ***continued from previous page.*** (B) An example of ELNES valence state fingerprinting (see Calvert et al. 2005). Fe $L_{2,3}$-edges from the minerals hematite and orthoclase (containing Fe^{3+} in octahedral and tetrahedral coordination respectively), and hedenbergite and hercyanite (both containing Fe^{2+} in octahedral and tetrahedral coordination respectively); the blue curves are the experimental EELS results while the green curves are the results of theoretical modeling using atomic multiplet theory (Brydson 2001; Ahn 2004). Note the shift to higher energy (from 707.5 eV to 709.5 eV) with increasing oxidation state of Fe. Theoretical data calculated by Derek Revill and Andrew Scott, University of Leeds.

quasiatomic transitions (so called since the observed ELNES is essentially atomic in nature and only partially modified by the crystal field due to the nearest-neighbor atoms). Examples of such spectra are provided by the $L_{2,3}$-edges of the 3*d* and 4*d* transition metals and their compounds and the $M_{4,5}$- edges of the rare-earth elements. These spectra exhibit very strong, sharp features known as white lines, which result from transitions to energetically narrow d or f bands. This makes detection and quantification of these elements extremely easy. Rather than using band structure calculations, such spectra are more appropriately modeled using atomic multiplet theory, in the presence of a crystal field of a particular ligand field symmetry. As an example, Figure 14 shows the $L_{2,3}$-edges from a number of manganese minerals, containing manganese in either the +IV, +III or +II oxidation state. Transitions from the Mn 2*p* shell are actually split into two components separated by the spin orbit splitting of the ionized 2*p* core level: an L_3-edge followed at higher energy loss by a broader L_2-edge. It is clear that both the L_3- and L_2-edges exhibit a chemical shift to higher energy loss with increasing manganese valence (this remains true when elemental manganese is also considered). Additionally, the relative intensities in the two separate white line components also clearly depend on the valence of the excited atom thus leading to the possibility of oxidation-state identification in an unknown sample. A mineralogical example of this type of analysis is provided by the study of chromium valence in hydrogarnets (Hiller et al. 2007).

Finally, EELS may be used to extract local structural information such as the length of chemical bonds. There are two approaches to bond-length determination: the first is to analyze the weak oscillations occurring ~40-50 eV above the edge onset known as extended energy loss fine structure (EXELFS—the electron equivalent of EXAFS in XAS). Since these oscillations are weak, high statistical accuracy (i.e., high count rates and long acquisition times) is required if useful information is to be extracted. The second procedure employs the energy position of

the broad ELNES peaks some 20-30 eV above the edge onset, known as multiple scattering resonances (MSR). As their name suggests, these features arise from a resonant scattering event involving the excited electron and a particular shell of atoms. The energies of these features above the edge onset have been shown to be proportional to $1/R^2$, where R is the bond length from the ionized atom. Identification of such MSR permits a semi-quantitative determination of nearest neighbor, and in some cases second nearest neighbor bond lengths (Kurata et al. 1993; see also Daniels et al. 2007).

EDX AND EELS IMAGING

As mentioned at the beginning of this chapter, besides simple analysis using a focused probe in say CTEM, using STEM it is possible to raster the electron probe across the specimen and record an EDX or EEL spectrum at every specimen pixel (x,y)—this technique being generally termed "Spectrum Imaging." The complete dataset may then be processed (either off- or increasingly on-line) to form a quantitative one dimensional line scan or two dimensional map of the sample using either standard elemental quantification procedures for elemental composition using either EDX (see for example Figs. 7 and 20) or EELS outlined previously. Alternatively the position and/or intensity of characteristic low loss or ELNES features may be used so as to obtain line scans or maps related to variations in chemical bonding (Egerton 2011).

Processing of any series of EDX or EELS line scans or maps may be done using a number of techniques including the construction of simple scatter plots and identification of data clusters or employing more detailed multivariate statistical analysis (MSA) methods to determine the significant principal components. Such methods can be used to highlight distinct chemical phases within a sample region either in terms of elemental concentrations (EDX or EELS), or even local coordinations or valence states of particular elements (EELS). MSA can also be used to identify the principal components identified as noise which can then be removed so as to regenerate a noise-reduced dataset (Egerton 2011). This processed dataset can improve element detectability and quantification as well as identification of changes in ELNES as a function of spatial coordinate. More recent developments in STEM spectrum imaging involve fully computerized beam control and beam blanking which allows complex, discontinuous areas in a microstructure to be scanned during the acquisition of a spectrum image (Sader et al. 2010).

Subject to the constraints of radiation damage, the inherent high spatial resolution of the EEL spectrum imaging technique has allowed maps of elemental distributions to be formed at sub-nanometer and even atomic resolution (Bosman et al. 2007). This is because EELS employs an aperture before the spectrometer and detector, which defines the collection angle (β) and can therefore be used to limit the region of the beam-broadened volume contributing to the recorded spectrum. Future developments will include the more routine production of atomic resolution chemical maps using variations in ELNES. Recently the possibility of near atomic resolution EDX maps has also been demonstrated (Watanabe 2009), despite the inherent problems of probe broadening in the specimen.

Finally, STEM/EELS spectrum imaging is directly comparable to direct energy filtered imaging in the CTEM (EFTEM). EFTEM involves the selection of specific energy loss electrons, or narrow range of energy losses (''an energy window''—typically between a few eV and a few tens of eV) from the transmitted electron beam via the insertion of an energy selecting slit after the EEL spectrometer (see Fig. 12 and see also Ahn 2004). This energy filter is then combined with subsequent image-forming optics. The spectrometer and post-spectrometer image-forming system may form part of a post column imaging filter or the microscope system may employ an in-column design with the EEL spectrometer and slit placed between the objective and projector lenses. Generally, EFTEM is better suited to mapping from larger fields of view with relatively short acquisition times than STEM/EEL spectrum imaging. The spatial resolution of EFTEM

is limited to about 1 nm or so which is poorer than that of EEL spectrum imaging, particularly since the development of aberration corrected probes.

Using only zero loss (elastically) scattered electrons to form EFTEM images and diffraction patterns increases contrast and resolution, allowing easier interpretation than with unfiltered data (see Fig. 12). Chemical mapping may be achieved by acquiring and processing images formed by electrons that have undergone either a specific low energy loss event (such as an interband transition or a plasmon event) or an inner-shell ionization event, using either the whole ionization edge or a specific ELNES feature indicative of a certain bonding characteristic. For the mapping of elemental distributions using EFTEM, two approaches are commonly employed:

1. jump-ratio mapping employs two energy windows and hence energy-filtered images, one positioned just before the ionization edge and one positioned just after the edge; the post-edge image is divided by a pre-edge image to produce a semi-quantitative map of the elemental distribution that is sensitive to small concentrations and is relatively free of noise and also diffraction contrast present in crystalline materials.

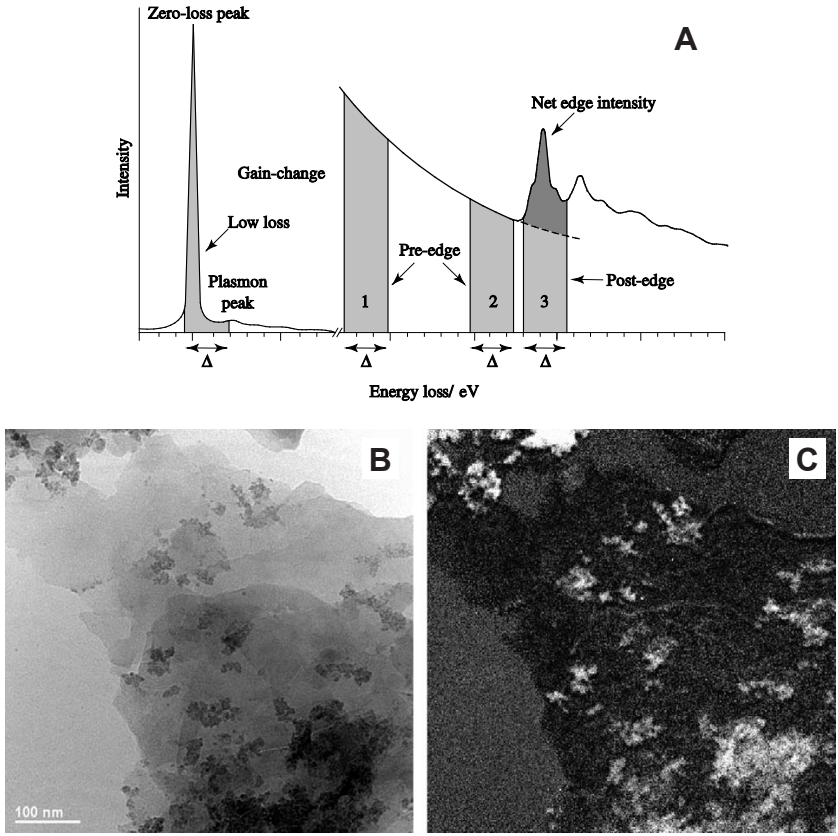

Figure 12. (A) Schematic diagram of EEL spectrum showing possible energy windows, of width Δ, used for energy filtered TEM imaging and mapping, (B) TEM bright field image and (C) corresponding Fe $L_{2,3}$-edge energy filtered EELS elemental (three window) map of a glacial sediment showing iron-rich nanoparticles (iron oxyhydroxides) on larger clay particles (from Raiswell et al. 2006).

2. true, quantitative elemental mapping (see Fig. 12C; Raiswell et al. 2006), where image intensity is proportional to concentration) usually employs three energy windows, two pre-edge windows and a post edge window; the two pre-edge images are used to extrapolate the background contribution to the post-edge image and this extrapolated background image is then subtracted from the post-edge image to produce a quantitative elemental map where image intensity is directly related to areal density.

Below we outline a practical application of TEM/EELS in mineralogical research.

EXAMPLE OF THE PRACTICAL APPLICATION OF EELS: EELS OF MANGANESE IN MINERALS AND ENVIRONMENTAL HEALTH

Introduction

Manganese is a 3*d* transition metal (TM) with the electron configuration [Ar]$4s^2 3d^5$. The partially-filled *d*-shells control the oxidation state of manganese which can exist in the formal oxidation states between 0 and +VII. In natural systems, manganese exists in the +II, +III and +IV valence states, often in multivalent minerals. In reduced igneous and metamorphic environments, manganese is most commonly +II and +III in solid solution with other transition elements in oxides, silicates and carbonates. Reviews of manganese occurrences in economically important deposits can be found in Huebner (1976), Roy (1968) and Hewett and Fleischer (1960). In more surficial environments, manganese is dominated by +III and +IV bearing oxides, but still may contain +II impurities. Manganese-oxides are found in mixtures of nanosized phases in various degrees of crystalline perfection in a wide variety of oceanic and terrestrial environments, such as soils, ocean floors, fresh-water sediments, and deserts. An important fraction of Manganese-oxides under oxic conditions may have formed from oxidation of Mn(II) by O_2 via microbially-mediated processes.

Although manganese-oxide minerals in the environment are generally far less abundant than other minerals, such as iron-oxides, the importance of manganese-oxides in controlling environmental chemical processes is not in accordance with their abundance (Post 1999). An important aspect of manganese-oxides is their capability to oxidize a wide variety of redox-active chemical species including many inorganic or organic contaminants in the environment, such as pharmaceuticals, metals and metalloids (Murray and Dillard 1979; Oscarson et al. 1981; Manceau et al. 1997; Fredrickson et al. 2002). The oxidation reactions can significantly impact the toxicity, bioavailability and mobility of the contaminants. Augmenting the high redox potential and extraordinary sorption properties is the high surface area of manganese oxides with nanoparticulate size. These characteristics make manganese-oxides one of the most important components of the aquatic and terrestrial ecosystems. An excellent review of the types and structures of manganese oxides in deposits and the environment can be found in Post (1999).

Analytical considerations for EELS determination of manganese valence

Manganese presents analytical considerations similar to its periodic table neighbors. Like other TM elements, manganese transitions accessible to EELS analysis include the *L* and *M* ionization edges. As with all the TM elements, the L_3/L_2 white-line transition ratio of Mn deviates from the expected value of 2 (Leapman and Grunes 1980). These deviations may be used to determine information about the coordination number and formal valence state. Unlike iron, which has only two valence states, manganese has the three common states listed above. However, the simultaneous coexistence of all three states has yet to be quantitatively addressed through EELS and current studies have only dealt with Mn(II)/Mn(III) and Mn(III)/Mn(IV) combinations.

Near edge structure of Mn $M_{2,3}$-edge

Little quantitative work has been done on the $M_{2,3}$ transitions of manganese. Early work was initiated by Rask et al. (1987) and Hofer and Wilhem (1993). Figure 13 illustrates the changes in the near-edge structure of the $M_{2,3}$ edge at about 50 eV for different valence states. They follow similar trends of iron (van Aken et al. 1999) in that the pre-peak intensity, position and ratio with the main peak is a function of oxidation state. Mansot et al. (1994) correlated the energy of both the maxima and the inflection point of the $M_{2,3}$ edge pre-peak. They were able to reproduce the mean valence value of manganese oxybromides within 4% relative error using these features.

The advantage of using the *M* edge relative to the Mn $L_{2,3}$ edge is that the *M* edge is more intense and the nearby zero-loss peak acts as a precise internal energy calibration. The disadvantage of the *M* edge is its proximity to the plasmon peak complicating background subtraction and it is highly affected by sample thickness. Another disadvantage of the *M* edge is the overlap of other TM elements commonly associated with manganese such as Mg *L* and Fe *M* (that are often in higher concentration than manganese). This limits the use of the *M* edge for quantification to simple, nearly pure, manganese minerals often only found in synthetic samples. Because of this, later methods for manganese valence determinations focused on the $L_{2,3}$ edge.

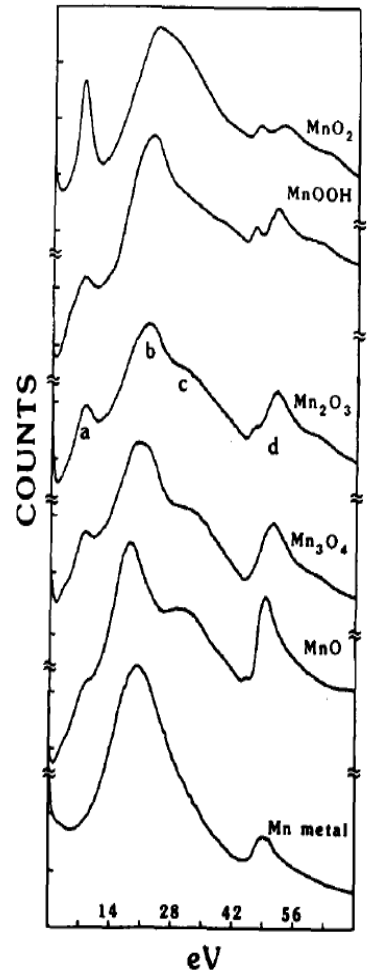

Figure 13. Low loss spectra of five manganese oxides and manganese metal. Included in this region are the plasmon peak (b) and the manganese $M_{2,3}$-peak (d) and interband transitions (a) and (c) all of which change with manganese oxidation state (from Rask et al. 1987).

Near edge structure of Mn $L_{2,3}$-edge

Early studies of the Mn *L* edge ELNES were done by Sparrow et al. (1984), Otten et al. (1985) and Rask et al. (1987) using a serial EEL spectrometer with a nominal resolution of ≥2 eV. Otten et al. (1985) and Rask et al. (1987) identified a chemical shift of $L_{2,3}$ edge with oxidation state to span approximately 4 eV between Mn(II) and Mn(IV). Subsequent reported absolute values of the L_3 edge for the three most common oxidation states for manganese vary considerably (Table 1). All three also reported a change in the L_3/L_2 ratio that decreased with increasing oxidation state in simple manganese oxides. From these initial studies, the usefulness of EELS for the determination of mean valence in minerals with mixed valence states was predicted.

Later, Garvie and Craven (1994a) and Garvie et al. (1994) used a parallel EEL spectrometer with a resolution of 0.3 eV that gave greater detail of NES. Twenty-five manganese-containing materials were studied covering oxidation states 0, +II, +III, +IV and +VII with different numbers of coordinating oxygen anions (Fig. 14). With respect to Mn(II), differences in the sharpness of the a and c peaks of L_3 edge for various Mn(II) minerals were apparent. Peak a

Table 1. Review of reported absolute energy loss values of the L_3 edge peak maxima for the three most common oxidation states for manganese (modified from Schmidt and Mader 2006)

Reference	Mn-L_3 energy-loss (eV)			
	Mn(II)	**Mn(III)**	**Mn(IV)**	**Δ(Mn(II)-Mn(IV))**
Mansot et al. (1994)	637.8	639.3	640.7	2.9
Paterson and Krivanek (1990)	639.0	639.6	642.1	3.1
Kurata and Colliex (1993)	639.5	642.0	643.0	3.5
Garvie and Craven (1993)	640	642	644	4
Loomer et al. (2007)	640.2	642	643.5	3.3
Schmidt and Mader (2006)	640.8	643.0	643.8	3
Laffont and Gibot (2010)	641.2	642.8	644.0	2.8
Rask et al. (1987)	642.4	643.8	646.4	4
Pecher et al. (2003)	639.7	641.35	643.05	3.35
Glatzel et al. (2004)	640.2	643.0	644.4	4.2
Average	640.1	641.9	643.5	3.4

is present in manganosite and rhodochrosite, but suppressed in MnF_2 and rhodonite or absent in lithiophilite, spessartine and jacobsite. It is apparent that the spectra are fingerprints for individual structures, but quantitative systematics for the bonding environment are lacking.

In the Mn(III) bearing minerals manganite, norrishite, gaudefroyite and bixbyite, Garvie and Craven (1994a) found that there were few differences between L_3 edges–even at high energy resolution. However, in Mn(IV) minerals, the L_3 edge contains 2 main peaks (a,b) and minerals studied are all similar in shape except for the sharpness of peak a. This distinction is reduced by spectrometers with lower resolution (e.g., 0.8 eV – Livi et al. 2012; 1.0 eV – Zhang et al. 2010; 1.6 eV – Loomer et al. 2007).

Mn(VII) in potassium permanganate has empty d-orbitals and is tetrahedrally coordinated. The spectrum obtained by Garvie and Craven (1994a) was sharp, but relatively featureless. Potassium permanganate proved to be extremely beam sensitive.

Quantification of valence by $L_{2,3}$-ELNES

Comparisons of four different methods for the extraction of the mean manganese valence from the $L_{2,3}$ white line intensities were made by Reidl et al. (2006). These methods—Pearson step function (Pearson et al. 1993), curve fitting, Walsh-Dray (Stolojan et al. 1999) and no subtraction—all differed in their handling of the subtraction of the continuum background and the integration of the white-line peaks. Reidl et al. (2006) found the Walsh-Dray method to be most precise in estimating the continuum background when analyzing $Mn(III)_2O_3$, $Mn(IV)O_2$ and $BaMn(VI)O_4$. Schmidt and Mader (2006) compared the relative precision of the white-line intensity ratio method as compared to the changes in the absolute energy positions of the peaks ($\Delta E(L_2\text{-}L_3)$). They concluded that although $\Delta E(L_2\text{-}L_3)$ changes systematically with mean valence, it has a greater error.

Loomer et al. (2007) studied the L_3/L_2 white line intensity ratio with the addition of internal energy calibration supplied by the Ti L_2 edge from added TiO_2 anatase nanocrystals. Although their resolution was relatively poor (1.6 eV resolution), they were successful at reproducing manganese valence within 3% error. Two aspects of this study are important: 1)

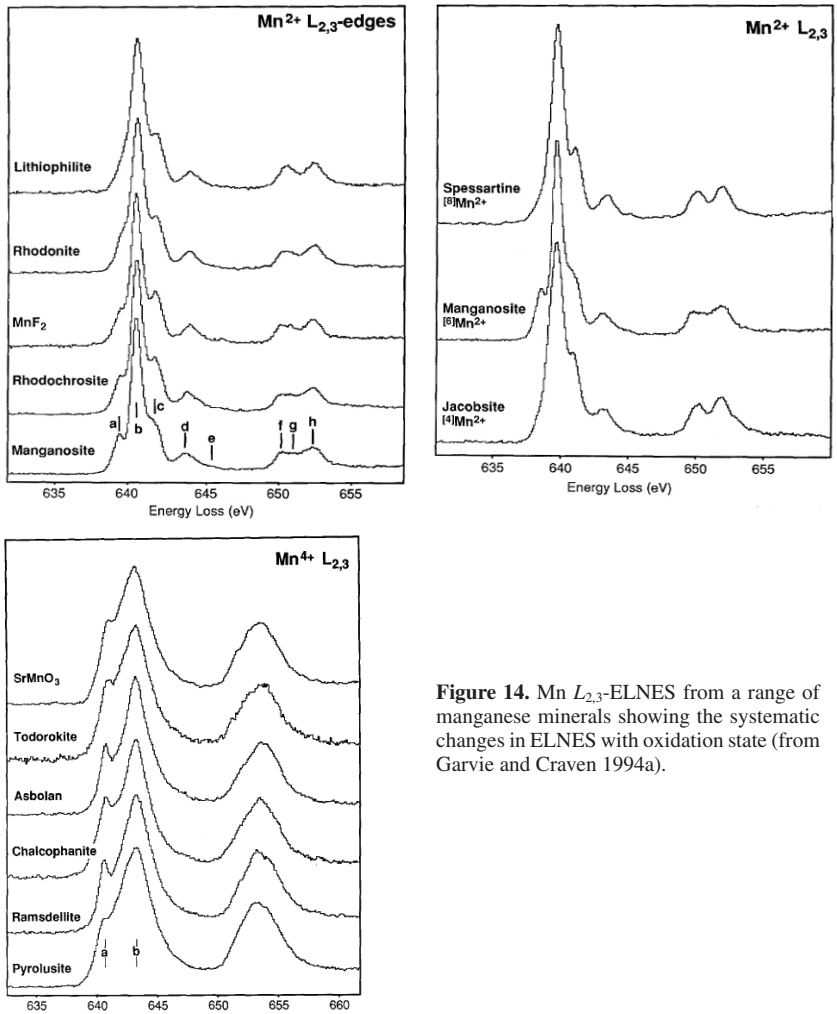

Figure 14. Mn $L_{2,3}$-ELNES from a range of manganese minerals showing the systematic changes in ELNES with oxidation state (from Garvie and Craven 1994a).

high-resolution EELS is not a requirement for successful EELS analysis of manganese valence if an internal energy standard is employed, 2) the L_3/L_2 white line intensity ratio flattens near the Mn(IV)-rich part of the calibration curve increasing the uncertainty in estimates dominated by Mn(IV) (Fig. 15) This is unfortunate since many environmentally important phases are rich in Mn(IV).

Zhang et al. (2010) assessed methods for determination of Mn(III)-Mn(IV) mixtures, and like Loomer et al. (2007), used an internal standard but in the form of Ti metal. This allowed for the examination of the O *K* edge without contamination of O from TiO_2. They compared $\Delta E(L_2\text{-}L_3)$, ΔE(Mn L_3-O *K*), the L_3/L_2 white line intensity ratio, Gaussian peak decomposition and multiple linear least-squares (MLLS) fitting of reference spectra methods. They concluded that of the calibration curve methods (first three methods), ΔE(Mn L_3-O *K*) was most precise (± 0.02 valence units). The failure of this method occurs when Mn is mixed with other oxide components and the position of the O *K* peak cannot be predicted. MLLS fitting results were subject to the selection of an appropriate standard, but yielded uncertainties (±0.03) that were

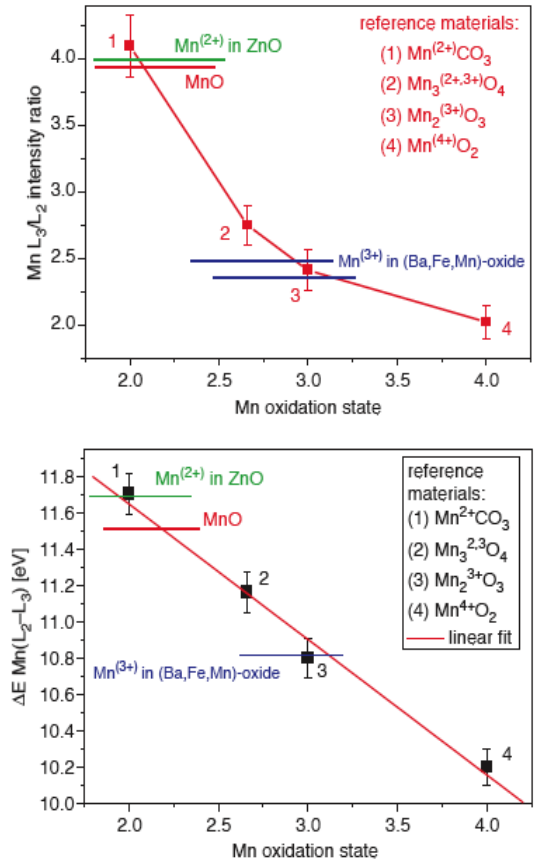

Figure 15. Calibration curves showing (*top*) Mn(L_3/L_2) white-line intensity ratio, and (*bottom*) Mn white line energy-difference ΔE Mn (L_2-L_3) versus Mn oxidation state in $MnCO_3$, Mn_3O_4, Mn_2O_3 and MnO_2 reference materials. The Mn(L_3/L_2) intensity ratios and energy-difference ΔE Mn (L_2-L_3) as measured in Mn-doped ZnO and (Ba,Fe,Mn) oxide are indicated by horizontal lines (from Schmidt and Mader 2006).

comparable to the ΔE(Mn L_3-O K) method without having to be pure manganese oxides. The Gaussian peak fit method was unsuccessful at modeling Mn(III)-Mn(IV) mixtures due to the similarity of shape and small separation of the Mn(III) and Mn(IV) L_3 peaks. Livi et al. (2012) followed Zhang et al. (2010) and used MLLS fitting methods to obtain average errors of ±0.05 (2σ).

Beam damage

Otten et al. (1985) was the first study to identify beam damage in manganese oxides during EELS analysis. This was corroborated and expanded upon by Garvie and Craven (1994c) for the phyllomanganate mineral asbolan. They conclude that damage of asbolan begins as a loss of oxygen on the surface of crystals and proceeds inward–progressively reducing the mean valence state. Evidence of loss of hydrogen from hydroxide minerals comes from an initial oxidation of manganese in $MnBO_2$ from Mn(II) to Mn(III) which was followed by a reduction back to Mn(II) as oxygen was subsequently lost (Garvie et al. 1994). Livi et al. (2012) determined the electron "safe dose" for beam sensitive todorokite and birnessite minerals. Accurate estimates of the mean valence values were possible for all varieties of birnessite minerals except for the

very poorly crystalline or amorphous δ-MnO_2. They point out that each variety of environmental mineral displayed a different damage profile, and every new study will require time-series analysis to determine the effects of beam damage. Future analysis of environmental minerals would benefit from advancements in low-dose imaging methods such as increased sensitivity of CCD cameras.

Applications

Varella et al. (2009) investigated the manganite (perovskite) $La_xCa_{1-x}MnO_3$ system with 2D atomic resolution. Although this is an engineered material, the study successfully demonstrated that the manganese mean valence could be measured on an atomic scale as La:Ca varied, and in some cases, could detect differences between non-equivalent O sites. The most precise estimate of manganese valence took advantage of systematic variations in the O K-ELNES main peak to pre-peak separation ($\Delta E\ K_M$-K_P). Luo et al. (2009) provided a theoretical basis for the correlation of $\Delta E\ K_M$-K_P with manganese oxidation state–although they conclude that $\Delta E\ K_M$-K_P is due to changes in the Ca:La proportion. Further empirical evidence that $\Delta E\ K_M$-K_P systematics may hold for simple manganese oxides may be found in Rask et al. (1987), Kurata and Colliex (1993) and Zhang et al. (2010). This has not been thoroughly studied and may not prove viable when other elements (such as Fe) are present.

Manganese nodules found at hydrothermal vents present a rich area for the application of EELS valence determination (see Hayes et al. 1985 for a description of the variety of manganese minerals found in Pacific nodules). However, this field has not been exploited as of yet. In one study, Buatier et al. (2004) performed an initial investigation of manganese valence in manganese crusts in active hydrothermal deposits on the flanks of the Juan de Fuca Ridge. Buatier et al. (2004) identified todorokite, birnessite and veil-like amorphous phases. EELS analysis showed the first two phases to have a mean valence of 3.7, while the amorphous material gave valences close to +II. Unfortunately, no time-series data were presented, so the validity of the low valence of the amorphous material is in question due to the likelihood of severe beam damage. The study does illustrate the value of combined X-ray diffraction, scanning electron microscopy, analytical TEM and EELS methods to identify all constituents of these complex mixtures, including amorphous material.

A preliminary report on EELS characterization of manganese minerals from the N'chwaning II mine in the Kalahari Manganese Field by Calvert et al. (2008) indicated that supposedly single valence mineral species were in fact of mixed valence.

The recent attention to the toxicity of manganese inhalation has led to some investigation of both the sources of manganese (e.g., welding fume) and its translocation to the central nervous system and other organs. Most analytical TEM studies of manganese in tissue employ the location of manganese through EDX analysis. However, there are two notable studies that use EELS. Richman et al. (2011) used STEM/EDX/EELS to characterize both the size and composition of manganese-weld fume. They demonstrated the usefulness of combining annular dark-field imaging to determine weld particle size/shape with EELS of oxygen, manganese and iron (major fume elements) and EDX of silicon and other minor elements (not readily accessible by EELS with 0.3 eV dispersion). The maps generated by EELS were far superior to those by EDX due to greater counting statistics. In addition, the O K-ELNES can also be used to deduce differences in crystal structure (rock salt vs. spinel). Richman et al. (2011) demonstrated that, in half the samples studied, there was a positive correlation of manganese content of breath exhale condensate with particle size in welders of the study group. The physicochemical properties of nanoparticles were important in understanding the amount of manganese delivered to the lungs, the depth to which nanoparticles will penetrate in the lungs, their residence time, and their surface area and reactivity. In this study, the statistically valid conclusion was drawn that smaller particles had longer residence time in the lung, while larger particles were exhaled more quickly.

Although manganese is found in all parts of the body, it is inhomogeneously distributed. Morello et al. (2008) investigated those areas in rats that have higher contents on the assumption that hyperaccumulation would occur during elevated manganese exposure. They used electron spectroscopy imaging in an in-column energy-filtering TEM to image high concentrations of manganese in mitochondria of astrocytes (glial nerve cells) and neurons, and to a lesser extent, in nuclei of astrocytes and neurons. This contrasted with biochemical assay results that suggested accumulation in nuclei. Morello et al. (2008) explain this discrepancy as a difference in spatial resolution between the two techniques. This application illustrates how EELS in the TEM can more accurately locate manganese accumulations in sub-cellular organelles than traditional biochemical assays. Developments in sample preparation methods (to minimize soluble manganese loss during fixing), cryo-analytical TEM preparation, and increased sensitivity of detectors will undoubtedly improve the quality of EELS applications to biological sciences in the future.

GENERAL APPLICATION OF EELS, SAED AND EDX

Finally we present an overview of the integrated use of the various imaging and spectroscopic techniques available in a modern analytical TEM to general mineralogical research.

The use of TEM for detailed mineral characterization accelerated rapidly in the 1970's with the development of ion beam milling for the preparation of electron transparent thin sections of rocks and minerals (see for example the review by Champness 1977). Since then, applications of TEM in the geosciences have kept abreast of the many developments in instrumentation, specimen preparation and analytical techniques (see for example, Lee 2010). It is now possible to image and chemically map a specimen atom column by atom column using spherical aberration corrected STEM combined with energy dispersive X-ray spectroscopy (EDX) (D'Alfonso et al. 2010) and/or electron energy loss spectroscopy (EELS) (Bosman et al. 2007). In order to achieve this resolution, one must prepare a suitably thin, representative specimen and control the applied electron dose in order to limit any irradiation induced artifacts (Egerton and Malac 2004; Egerton et al. 2010).

Most modern TEMs can readily provide atomic lattice imaging and, when equipped with the appropriate spectrometers, chemical information at the nanoscale if not the atomic. Identification of nanoscale segregation of elements within earth and planetary materials can bring new insight into the dynamic processes these materials undergo. Here we highlight recent examples of the characterization of environmentally important nanoparticle systems while highlighting a consistent theme of representative specimen preparation and analysis.

Use of (S)TEM to assess transport and retardation mechanisms of trace metal contaminants

Nanoparticles and colloids are a consistent feature of low temperature surface waters and ground waters. They remain suspended and are transported in moving groundwater and have a high surface area such that a relatively insoluble metal can be readily adsorbed onto the NP/colloid surface. Thus nanoparticles play a critical role in the transport of trace metal contaminants and it is therefore key to understand the binding sites of these colloids in order to further understand trace metal transport and retardation. Over the years there have been relatively detailed analyses of nanoparticle characteristics, with analytical STEM and CTEM emerging as powerful tools for the identification and characterization of trace metal contaminants on and within nanoparticulate phases. CTEM alone has been used to identify particles bearing toxic elements (Hochella et al. 1999; Suzuki et al. 2002) while analytical STEM combined with CTEM have been used to identify and characterize nanoparticulate

metal contaminants in a range of environmental, colloidal matrices (Utsunomiya and Ewing 2003; Utsunomiya et al. 2009). Using CTEM to identify contaminants in low concentration and localized to a nanoparticulate phase is limited because the image contrast alone will not identify the contaminant. The full analytical capability of the STEM however is very useful since the strong electron scattering of the contaminant metal can be used to identify (by HAADF-STEM) and map (by STEM-EDX or by CTEM-EFTEM) the metal contaminants in or on host particles. Subsequent CTEM (lattice imaging, electron diffraction and EELS) can be used to identify the speciation and crystal phase of the two.

In general, analytical S/TEM analysis is not used as a standalone characterization technique but more often it can provide nanoscale information to support bulk analytical data. For example (see Fig. 16), the identification of Cr(III) substitution in hematite within samples from the Ajka red mud spill site, Hungary relied on a combination of CTEM-selected

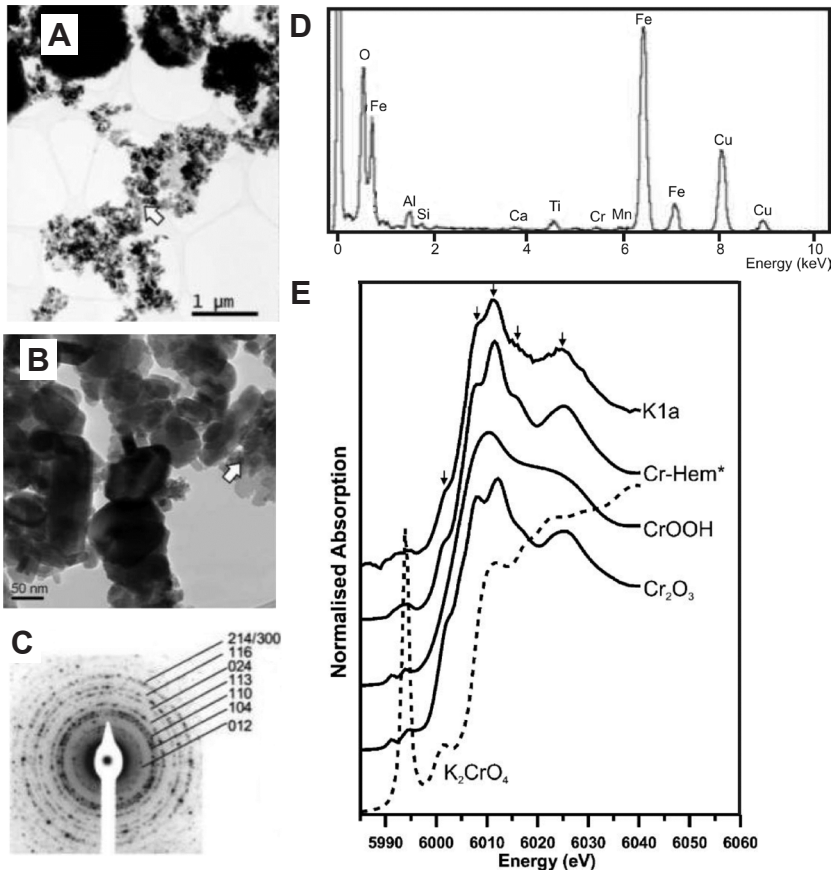

Figure 16. Identification of Cr(III) substitution in hematite within samples from the Ajka red mud spill site, Hungary (after Burke et al. (2012). (A) Low-resolution bright field TEM image of the red mud particles from the spill site. (B) Higher magnification image of area highlighted by white arrow in A. (C) Polycrystalline selected area electron diffraction pattern indexed to hematite. (D) EDX spectrum collected from the point shown with a white arrow in B, confirming the additional presence of Ti and Cr in the hematite phase. (E) Normalized Cr *K*-edge XANES spectra collected from the red mud sample (K1a) and three Cr(III) and one Cr(VI) containing standards. The spectrum from the red mud is consistent with the spectra collected from the Cr(III)-substituted hematite and Cr_2O_3 standards.

area electron diffraction and spot EDX analysis to identify Cr within a fine-grained hematite structure and X-ray absorption spectroscopy to identify the valence state of the Cr (Burke et al. 2012).

Similarly X-ray Absorption Spectroscopic (XAS) analysis of soils from a chromite ore processing residue disposal site indicated Cr is present as a mixed Cr(III)-Fe(III) oxyhydroxide phase and this was confirmed by STEM-EDX and BF-TEM imaging (Whittleston et al. 2011). The retention of Cr(III) within the soil was shown to be due to reductive precipitation of Cr(VI) by Fe(II).

Indeed, multiple approaches are essential to understanding metal speciation in complex heterogeneous sediments given the wide concentration range relevant to contaminated natural and engineered environments. For example (see Fig. 17 the association and speciation of the fission product, technetium-99, found in radioactive wastes, was examined under reducing conditions over a range of concentrations in estuarine sediments (Burke et al. 2010; Lear et al. 2010). Anoxic incubation experiments were conducted with direct (transmission electron microscopy and gamma camera imaging) and indirect (incubation experiments and chemical extractions) experimental techniques employed. The combination of low and high concentration measurements supported the hypothesis that removal of Tc from solution may be controlled by reduction of Tc(VII) to Tc(IV) by biogenic Fe(II) in sediments. STEM-EDX and TEM-EELS were employed specifically to show that the Tc was localized and co-associated with nanometer size Fe(II)-rich particles in the relatively high concentration sediments.

The multiple approaches are equally applicable to a biological setting. For example (see Fig. 18), evidence for a Si-specific intracellular mechanism for Al detoxification in aquatic snails, involving regulation of orthosilicic acid [$Si(OH)_4$] was supported by intracellular identification of hydroxyaluminosilicates (HAS) in exposed snails by analytical STEM (White et al. 2008). In snails preloaded with $Si(OH)_4$, behavioral toxicity in response to subsequent exposure to Al was abolished. Similarly, recovery from Al-induced toxicity was faster when $Si(OH)_4$ was provided, together with rapid loss of Al from the major detoxificatory organ (digestive gland). Temporal separation of Al and Si exposure excluded the possibility of their interaction ex vivo. Elemental mapping using analytical STEM and CTEM revealed nanometer-scale co localization of Si and Al within excretory granules in the digestive gland, consistent with recruitment of $Si(OH)_4$, followed by high-affinity Al binding to form particles similar to allophane, an amorphous HAS.

This work highlights the value of analytical STEM to the emerging field of nanoparticle toxicology where one of the goals is to assess the impact of engineered nanoparticles on the environment. For example, Ag nanoparticles are now extensively produced and used in consumer products and sulfidation is thought to be the dominant degradation product as they are released into the environment (Levard et al. 2011). Silver sulfide (α-Ag_2S) nanoparticles have been identified in the final stage sewage sludge materials of a full-scale municipal wastewater treatment plant using analytical STEM (Kim et al. 2010).

Developments in TEM specimen preparation

The crossover of geological and biological specimens also requires consideration of the recent developments in specimen preparation for TEM. Most nanoparticle work relies on drop-casting particles or particle suspensions directly onto amorphous carbon (or sometimes silicon or silicon nitride) support films for TEM. For valuable or potentially toxic particulates one can also use resin impregnation of a suspension and then after hardening, thin sections can be cut for TEM by an ultramicrotome (for example Burke et al. 2010). The drop-casting method is simple and can be used following the completion of solution based reactions to chart the progress of a reaction (for example, Penn and Banfield 1998). More recent developments are taken from biological specimen preparation where thin layers of particle suspensions are rapidly frozen

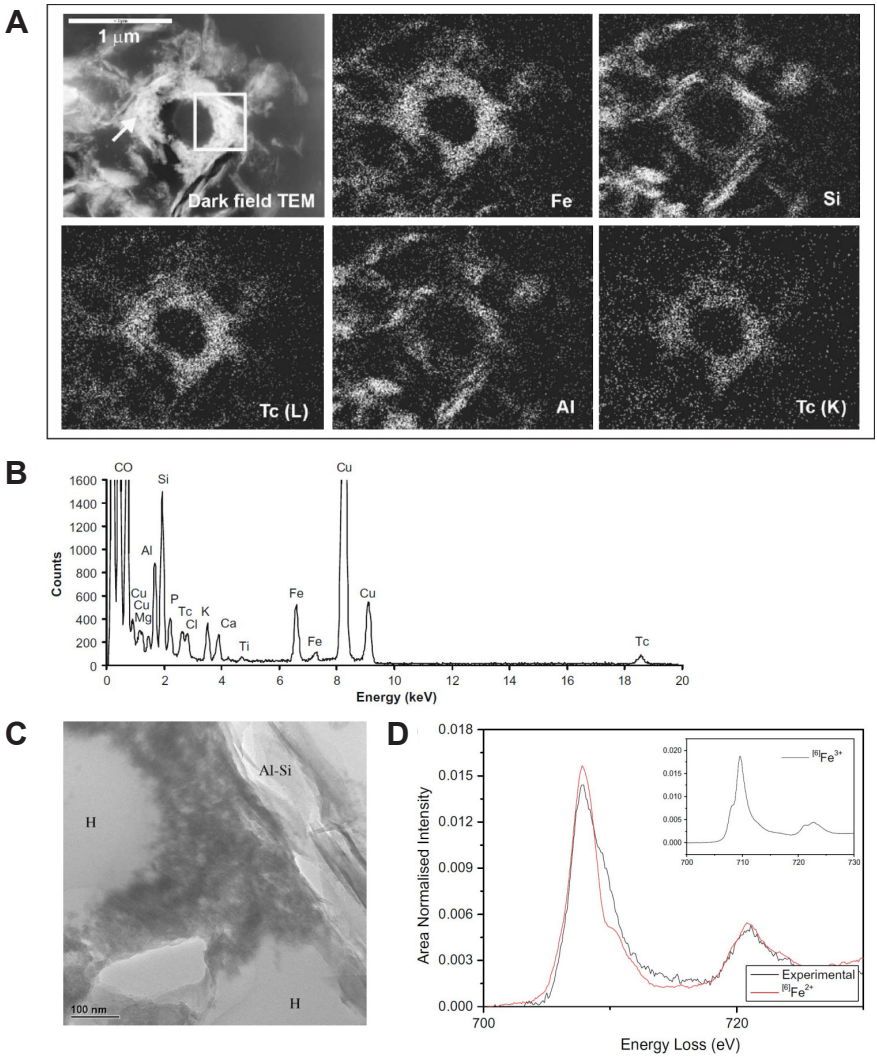

Figure 17. Identification of the association of the fission product, technetium-99, in estuarine sediments examined under reducing conditions (after Burke et al. 2010). (A) Annular dark field STEM image and elemental X-ray maps showing the distribution of Fe, Si, Al and Tc (L_α and K_α X-rays) in sediments incubated with 0.5% (w/w) Tc. Clearly, Tc is co-localized with Fe, and Si is co-localized with Al. (B) EDX spectrum of the whole region shown in A. Cu and C peaks are present due to stray X-rays emitted by the TEM grid and films, respectively. Tc L_α X-rays at 2.42 keV are indistinguishable from S K_α X-rays at 2.31 keV, but Tc K_α X-rays at 18.38 keV do not overlap in energy with any other elemental X-rays measured here, confirming the presence of Tc. (C) Bright field TEM image of the sediment shown to be Fe- and Tc-rich (inside white box in A showing a network of fine particles that are amorphous (by electron diffraction) next to larger Al and Si-rich crystals. (D) Background stripped Fe $L_{2,3}$-edge electron energy loss spectrum (black line) acquired from the Tc-rich region. The general shape of the edge and the position of the L_3 peak maxima (at 707 eV energy loss) is consistent with a spectrum from an Fe(II) rich region. For reference a spectrum from a well characterized Fe(II) bearing mineral (hedenbergite; $CaFe\text{-}Si_2O_6$, where the Fe is octahedrally coordinated to O) is shown in red and inset is a reference spectrum from a well characterized Fe(III) bearing mineral (hematite; $\alpha\text{-}Fe_2O_3$).

in solution allowing the hydrodynamic state of the particles and agglomerates to be observed (Hondow et al. 2012). These cryo-quenching approaches and subsequent TEM imaging and analyses recently helped quantify in a time resolved manner the kinetics and mechanisms of several geological relevant reactions (e.g., Tobler et al. 2009; Van Driessche et al. 2012). In the geosciences, recent developments include the use of TEM imaging to track and quantify the kinetics of nanoparticle formation and transformation. For example, conventional and cryo-TEM imaging helped quantify the nucleation and growth of amorphous silica (Tobler et al. 2009). Similarly, using TEM imaging, SAED and associated pair distribution quantifications, the formation and aging of nanocrystalline iron sulfide phases (amorphous FeS, machinawite, greigite and pyrite; Csákberényi-Malasics et al. 2012), which control the biogeochemical cycling of iron and sulfur in anoxic and suboxic marine sediments has been quantified. Finally, only by using novel fast-quenching techniques combined with high-resolution TEM imaging combined with EDX and SAED could the processes that control the nucleation, growth and transformation of calcium sulfate phases from aqueous solution be evaluated (see Fig. 19; Van Driessche et al. 2012). These studies showed that not only important geological processes but also crucial industrial applications can be accurately studied using the novel imaging, sample preparation and analytical approaches developed in the last few years.

Liquid cell imaging within the TEM is also progressing rapidly however the attainable spatial resolution still remains significantly less good than that available by CTEM (Klien et al. 2011). Finally, FIB sectioning of TEM specimens has been used to successfully examine mineral weathering products (Lee et al. 2007) and the interface between microbes and minerals (Obst et al. 2005; Bonneville et al. 2009). Avoiding preparation artifacts such as over-thinning with the ion beam and bending of the samples is a major issue with these types of samples. As section depth increases, it becomes more difficult to keep the sides flat, and over-thinning of certain areas can occur because the profile of the ion beam itself is not parallel and this has to be accommodated by tilting the face of the section to be milled a few degrees off axis from the incident ion beam (Ishitani et al. 1994). Deep sections also have less support, and non-rigid materials such as the cellular components of the above samples can bend. Once this occurs protruding "bulges" will be milled away more quickly than the rest of the section, potentially leaving holes (Ward et al. 2013). This can be avoided by leaving relatively thick sections (say 100-150 nm) however this should be balanced against the required spatial resolution of the (S)TEM analysis (for example, the spatial resolution obtainable by EDX decreases with increasing specimen thickness because of the increased interaction volume that generates X-rays from the incident beam in the thicker sections; Williams and Carter 1996).

FIB-preparation of very thin sections suitable for atomic resolution HAADF-STEM, with parallel sides and a sample depth of 2 to 3 μm have been successfully achieved (Bals 2007; Schaffer 2012). Recently, analytical TEM of FIB prepared mineral-fungi sections has been used to demonstrate weathering of natural minerals (biotite) by fungal hypha, with the conclusion that this proceeds by a combination of biomechanical forcing and chemical dissolution (Bonneville et al. 2009). For the case of Bonneville et al. (2009), careful FIB preparation followed by analytical TEM has demonstrated that weathering of biotite by fungal hypha proceeds by a combination of biomechanical forcing and chemical dissolution. Here (see Fig. 20), CTEM and SAED analysis of the fungus-biotite interfaces revealed intimate fungal mineral attachment, biomechanical forcing, and altered interlayer spacings while STEM-EDX identified substantial depletion of potassium (~50 nm depth) with STXM analysis of the same sections showing oxidation of the biotite Fe(II) and finally CTEM once again showing the formation of vermiculite and clusters of Fe(III) oxides. Modeling of the nanometer-scale elemental fluxes obtained at the hypha-mineral interface by STEM-EDX demonstrates how the weathering of rocks may be accelerated to release nutrients to plants (Bonneville et al. 2011).

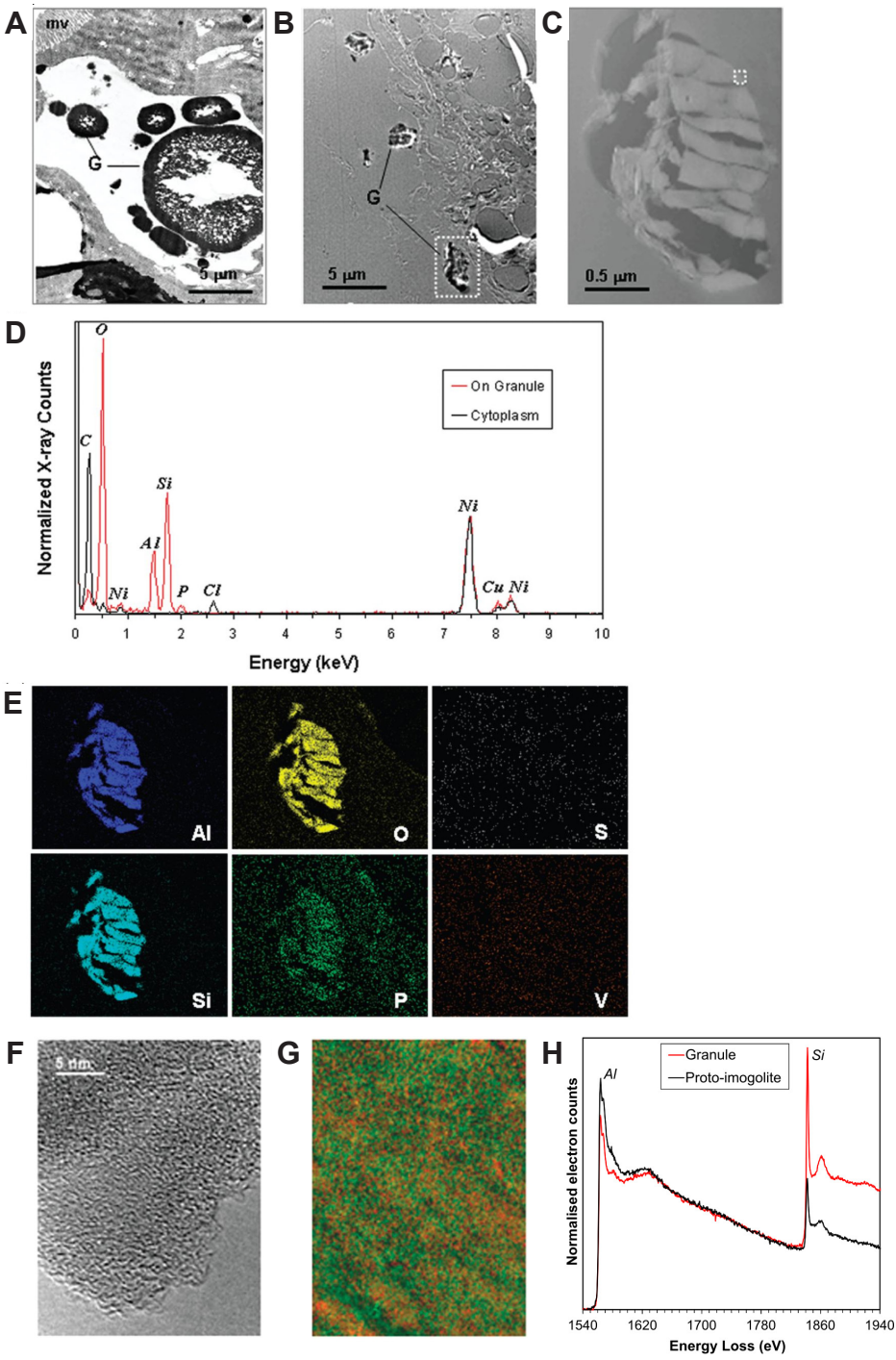

Figure 18. *caption on next page*

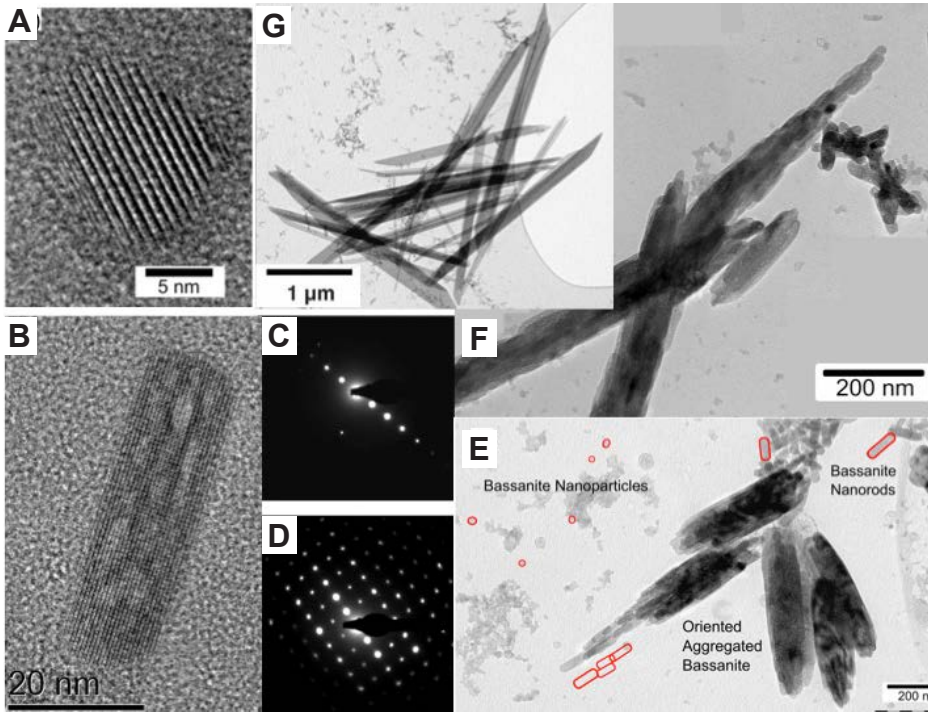

Figure 19. Using fast and time-resolved sample quenching and associated TEM imaging and analyses Van Driesche et al. (2012) have documented how a geologically important mineral phase, gypsum, forms from aqueous solutions via a multi-stage reaction chain. In a first step the homogeneous precipitation of nanocrystalline (A) calcium sulfate hemihydrate, bassanite ($CaSO_4 \cdot 0.5H_2O$) occurs; interestingly at this nanoscale this happens below its predicted solubility. The so formed rounded nanocrystals transform to bassanite nanorods (B) with corresponding SAED pattern in (C). These nanorods later self-assemble into aggregates that are co-oriented along their *c*-axis (E) and corresponding SAED pattern in (D). These oriented aggregates develop into overall morphologies reminiscent of the dihydrate gypsum ($CaSO_4 \cdot 2H_2O$), yet crystallographically they are still just self-assembled oriented bassanite nanorods (F). Only in a final stage, do these bassanite aggregates hydrate to transform to gypsum crystals (G).

Figure 18 (*on facing page*). Evidence for a Si-specific intracellular mechanism for Al detoxification in aquatic snails, *Lymnaea stagnalis* (after White et al. 2008). (A) Digestive gland thin sections were taken from snails exposed to Al (500 µg L^{-1}) for 15 days and stained with heavy metals to show membrane-bound granules (G) in an excretory cell, bordered by microvilli (mv). (B) Unstained section (for elemental analysis) with granules still evident. (C) Bright-field STEM image of granule outlined in B. (Some diamond knife damage during sectioning is evident). (D) Spot EDX spectra from the granule and the surrounding cytoplasm showing the granule composition to be consistent with an aluminosilicate phase containing some phosphorus. The counts are normalized to the background signal from the Ni support grid. (E) STEM-EDX maps of the granule shown in C, demonstrating the co-localization of Al, Si, O, and minor amounts of P. S and V (negative control) were not detected. (F) TEM image of the area outlined in C, indicating that the granule is non-crystalline. (G) EF-TEM false colour elemental map shows nanoscale co-localization of Al (red in electronic version) and Si (green in electronic version) [both Al and Si are light grey in print version]. (H). Al *K*- and Si *K*-edge electron energy loss spectra from a digestive gland granule (red in electronic version and grey in print version) and from synthetic proto-imogolite (black in both electronic and print versions): gift from Dr. D. Lumsdon, The Macaulay Institute, Aberdeen). Similarity in shape of the Al *K*-edges suggests that the allophane phase of the granule is similar in structure to proto-imogolite.

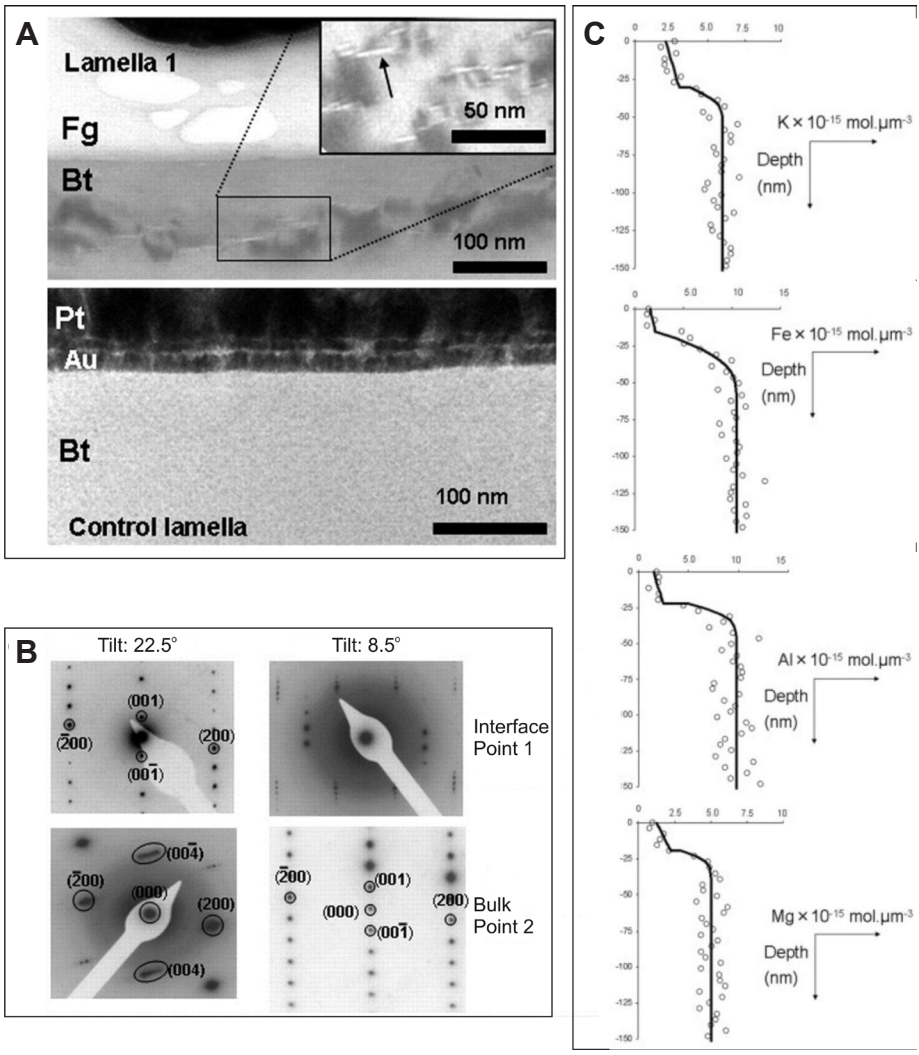

Figure 20. Evidence for biomechanical forcing and chemical dissolution, weathering of biotite by fungal hypha (after Bonneville et al. 2009). (A) BF-TEM image of the cross-section of a hypha (Fg)-biotite (Bt) interface, labeled lamella 1 and compared to a cross section of pristine biotite, labeled control lamella. Both cross-sections were prepared by focused ion beam milling. Strong diffraction contrast and micro-cavities (image inset) are visible in the biotite incubated with the fungal hypha and indicate physical alteration of the mineral. (B) Selected area electron diffraction patterns of the interfacial versus bulk biotite in lamella 1 indicate a misorientation of the biotite at the interface compared to that in the bulk (indexed to biotite monoclinic structure; JCPDS reference 01-074-2578). The biotite crystal structure was tilted from a relative angle of 8.5° in the bulk (point 2) to an angle of 22.5° at the interface with the hypha tip (point 1) to obtain the same $[0\bar{1}0]$ zone axis diffraction patterns. (C) STEM-EDX derived elemental (symbols) and modeled (lines) concentration depth-profiles over the 150 nm below the hypha-biotite interface for K, Al, Fe and Mg in a FIB section exposed to a fungal hypha for ~ 70 days, demonstrating clear chemical alteration of the biotite (Bonneville et al. 2011).

Developments in analyzing poorly crystalline, beam sensitive materials

It is well known that the electron beam in a TEM/STEM may cause some form of specimen alteration during examination and may affect the integrity of the information sought from the specimen (Hobbs 1987; Egerton and Malac 2004; Reimer and Kohl 2008). For example, in the last section we discussed the FIB preparation and analysis of biotite, which is sensitive to damage by the high energy electron beam of the TEM (Bell and Wilson 1981). At 300 keV, mass loss occurs as a function of accumulated electron fluence (Ma et al. 1998) and this is therefore a major concern when using the focused probe of a STEM (operating at 197 keV in the case of Bonneville et al. 2009). There are reports of a threshold dose for electron beam induced damage of minerals such as vermiculite (Baumeister and Hahn 1976) and a threshold fluence for a biotite has also recently been identified (Ward et al. 2013). This has been obtained following a cumulative electron fluence protocol developed for the TEM-EELS analysis of ferritin and ferrihydrite (Pan et al. 2006, 2010) and for the STEM-EDX analysis of hydroxyapatite nanoparticles (Eddisford et al. 2007). Furthermore, similar time dependent exposure of amorphous calcium carbonate (ACC) nanoparticles to a high voltage electron beam (200 keV) immediately induced the formation of 2-5 nm ordered subdomains, which grew and transformed into larger (5-20 nm) crystalline domains (Fig. 21; Rodriguez-Blanco et al. 2008). This process occurred within the confinement of the large spherical ACC nanoparticles and this crystallization is likely the results of dehydration of the initially highly hydrated ACC. However, the nature of the resulting crystalline domains (i.e., whether they correspond to 'proto-vaterite' or proto-calcite' is unclear as the mechanisms of this beam-induced crystallization may differ from that occurring in aqueous solution (Rodriguez-Blanco et al. 2011). A quantitative understanding of the stability and transformation mechanisms of ACC into geologically stable calcium carbonate polymorphs has major implications for biomineral formation, which themselves often form from an initial hydrated ACC. For example, the formation of coccoliths and foraminifera, the dominant calcium carbonate biominerals in our world's oceans, controls the global carbon cycle. Using novel imaging and analytical techniques as described above can help us better understand how the formation of such biominerals may be affected by for example changes in climate (i.e., increase in atmospheric pCO_2 and associated ocean acidification).

As indicated above, near-edge core-excitation spectroscopy, such as energy loss near-edge structure (ELNES) analysis, has been demonstrated as a useful tool for studying mineral oxidation states and coordination environments (Garvie et al. 1994, 2004; Garvie and Craven 1994b). Fe $L_{2,3}$-ELNES specifically has been used to investigate the effects of electron dose (via control of electron fluence) in hydrated iron phosphate, ferrihydrite and ferritin/haemosiderin cores in an iron- overloaded human liver biopsy (see Fig. 22) and the results demonstrate the reduction of iron and its transformation from octahedral to tetrahedral co-ordination under progressively increasing electron dose, consistent with the preferential loss of iron coordinating ligands (O, OH and H_2O) (Pan et al. 2010).

By considering the cumulative effect of electron fluence on a mineral, one can extrapolate back to the pristine structure or chemical state and, for the case of ferrihydrite (Fh), this characterization is very topical because of the potential presence of 'coordination under saturated' tetrahedral ferric iron sites. First described in 1967, there is still some controversy over the precise atomic structure of Fh because its size and defective nature make a definitive characterization challenging. One structural model, proposed in 1993 and based on powder XRD analysis, describes Fh as three intermixed phases where iron occupies octahedral interstices only (Drits et al. 1993). Recently (2007-2010), a new model challenging the standard view has been proposed, based predominantly on structural refinement of atomic pair-distribution functions (PDF) measured in the synchrotron using total X-ray scattering (Michel et al. 2007, 2010). Fh is described in this model as a single phase in which iron

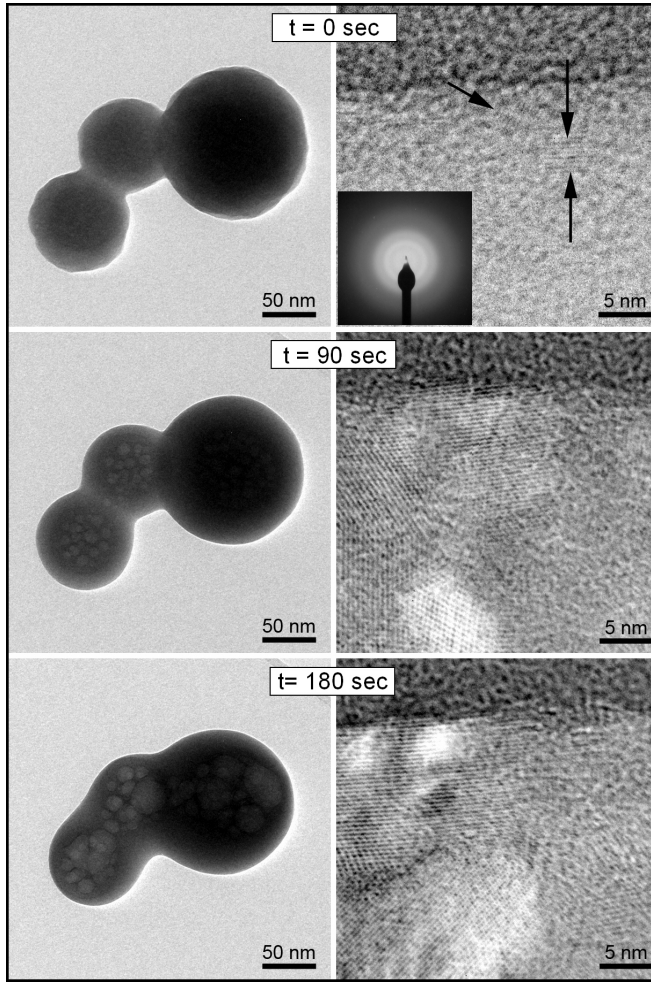

Figure 21. Bright field TEM image time series of the crystallization of amorphous calcium carbonate (ACC) upon exposure to the electron beam. From top to bottom, changes in ACC morphology (*left*) and internal structure and ordering (*right*) as a function of time. The insert in the upper right image shows a SAED pattern of ACC revealing only diffuse rings related to poorly ordered materials (from Rodriguez-Blanco et al. 2008).

occupies both tetrahedral (≤ 10-20%) and octahedral interstices. This new model has received some criticism (Rancourt and Muenier 2008; Manceau 2009, 2010, 2011, 2012; Barron et al. 2012) and additional support (Maillot et al. 2011; Xu et al. 2011; Harrington et al. 2011; Peak and Regier 2012; Guyodo et al. 2012). The TEM measurement of Fe $L_{2,3}$-ELNES from 6-line Fh has contributed to this debate however it has not provided a definitive measure of the tetrahedral iron content because of the uncertainty in the extrapolation back to very low electron fluence (Pan et al. 2010).

More recently, Vaughan et al. (2012) have shown X-ray scattering profiles of synthetic 2-line ferrihydrite that are consistent with other reports for ferrihydrite. The measurement of ~93% octahedrally coordinated ferric iron by extrapolation of the Fe $L_{2,3}$-ELNES to very

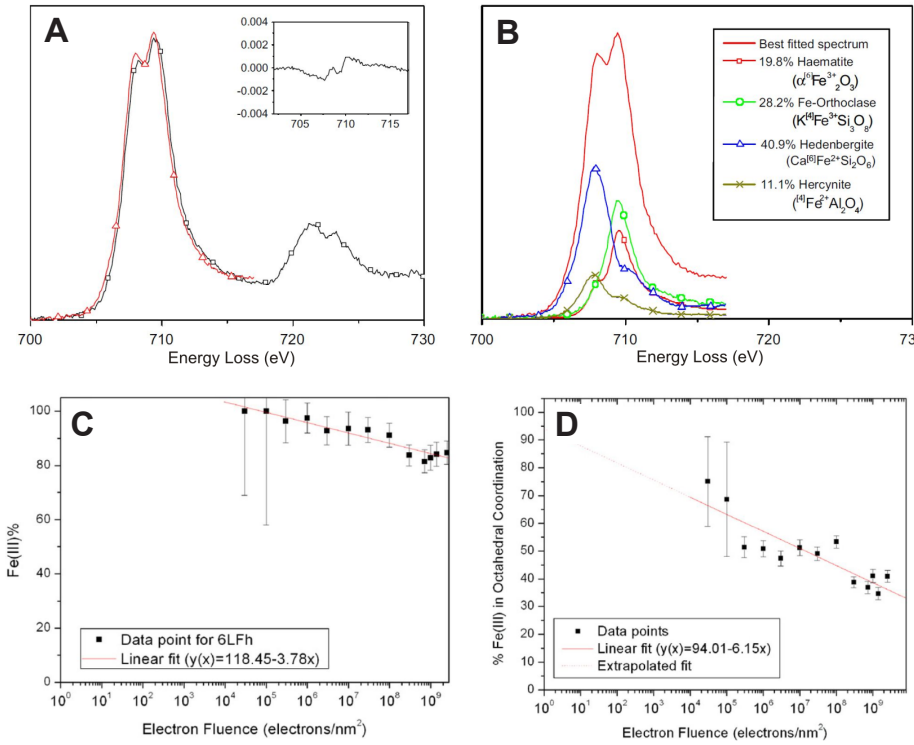

Figure 22. Fitting Fe $L_{2,3}$-edge TEM EEL spectra to estimate the octahedral ferric Fe content of ferrihydrite (after Pan et al. 2010). (A) An example of the result of a non-linear least squares (NLLS) fitting to a Fe L_3-energy loss edge (i.e., 702-717 eV energy loss) of iron phosphate dihydrate. The experimental spectrum is black and the best fit spectrum is red. The inset shows the residual intensity following subtraction of the best fit curve. (B) The relative proportions of the four reference spectra that, when combined, produce the best fit to the experimental spectrum. (C) The NLLS fitting coefficient estimate of the percentage content of total ferric iron (octahedral + tetrahedral coordination) in 6-line ferrihydrite (6LFh) at each accumulated electron fluence. (D) The estimated percentage of octahedrally coordinated ferric iron in 6-line ferrihydrite at each accumulated electron fluence. The extrapolated ferric and octahedral content at very low fluence are 100% and 95% respectively.

low electron fluence is not, however, in complete agreement with the most recently proposed structural model described above (see Fig. 23). Nitrate has also been detected and inferred to be a surface contaminant, because its presence does not apparently affect the bulk structure. It may be that the incorporation of nitrate affects the surface co-ordination states of the iron and so the measurement of tetrahedral iron. This highlights the need for careful and consistent synthesis and characterization of ferrihydrites before comparison with structural models is made.

CONCLUSIONS

This review of the chemical analysis of mineralogical micro- and nano-structures *in situ* within the transmission electron microscope has highlighted the two major techniques of energy dispersive X-ray analysis and electron energy-loss spectroscopy.

This article has summarized the basic aspects of the excitation mechanisms, the interpretation, the acquisition and processing of both EDX and EELS spectra. Details of instrumenta-

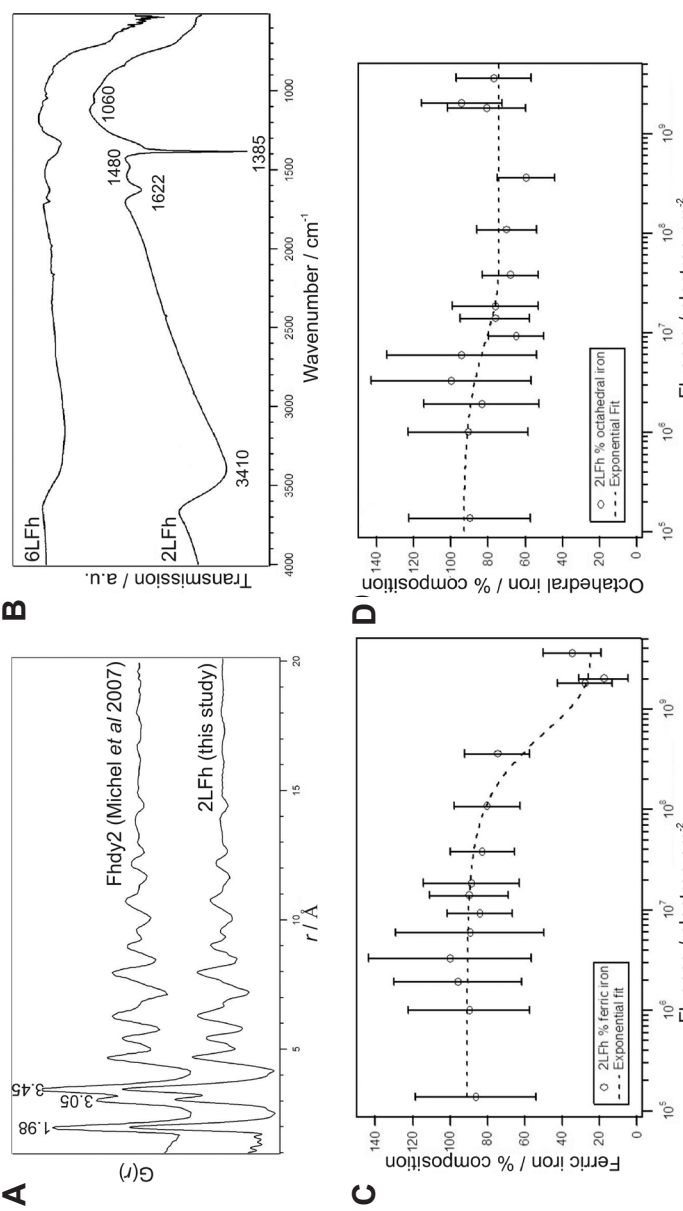

Figure 23. Characterization of 2-line ferrihydrite (after Vaughan et al. 2012). (A) Comparison of the total X-ray scattering pair distribution function data for 2-line ferrihydrite produced by Vaughan et al. (2012) to that produced by Michel et al. (2007). The atom-atom separations of the first three correlations, are labeled in units of Å. The profiles of the two samples are very similar. (B) Fourier transform infrared spectra obtained from 2 and 6-line ferrihydrite produced by Vaughan et al. (2012). The 2-line ferrihydrite has a steeper background and a sharp peak at 1385 cm^{-1} that can be attributed to nitrate. Fe-L_3 ELNES analysis of the ferric (C) and octahedral (D) iron content of 2-line ferrihydrite as a function of cumulative electron fluence, following the procedure of Pan et al. (2010). The extrapolated ferric and octahedral content at very low fluence are 91% and 93% respectively.

tion have been discussed including the practical usage of the techniques as applied to minerals together with the types of chemical information that can be extracted. This has been facilitated by the provision of a limited set of examples, although it should be stressed that the interested reader should consult the references within this review and further reading material for a much more complete list of potential applications. In addition, we have attempted to highlight the benefits (and in some cases complications) introduced by the use of small, highly converged, aberration corrected probes.

REFERENCES

Ahn CC (ed) (2004) Transmission EELS in Materials Science, 2nd Edition. Wiley, Weinheim

Ankudinov AL, Ravel B, Rehr JJ, Conradson SD (1998) Real space multiple scattering calculation of XANES. Phys Rev B 58:7565-7576. See also *http://leonardo.phys.washington.edu/feff/*

Bals S, Tirry W, Geurts R, Yang Z, Schryvers D (2007) High-quality sample preparation by low kV FIB thinning for analytical TEM measurements. Microsc Microanal 13:80-86

Bangert U, Harvey AJ, Schreck M, Hörmann F (2005) Extended defect related energy loss in CVD diamond revealed by spectrum imaging in a dedicated STEM. Ultramicroscopy 104:46-56

Barron V, Torrent J, Michel FM (2012) Critical evaluation of the revised akdalaite model for ferrihydrite — Discussion. Am Mineral 97:253-254

Baumeister W, Hahn M (1976) An improved method for preparing single crystal specimen supports: H_2O_2 exfoliation of vermiculite. Micron (1969) 7:247-251

Bell LA, Wilson CJL (1981) Deformation of biotite and muscovite: TEM microstructure and deformation model. Tectonophysics 78:201-228

Bonneville S, Smits MM, Brown A, Harrington J, Leake JR, Brydson R, Benning LG (2009) Plant-driven fungal weathering: Early stages of mineral alteration at the nanometer scale. Geology 37:615-618

Bonneville S, Morgan DJ, Schmalenberger A, Bray A, Brown A, Banwart SA, Benning LG (2011) Tree-mycorrhiza symbiosis accelerate mineral weathering: Evidences from nanometer-scale elemental fluxes at the hypha-mineral interface. Geochim Cosmochim Acta 75:6988-7005

Bosman M, Keast VJ, García-Muñoz JL, D'Alfonso AJ, Findlay SD, Allen LJ (2007) Two-dimensional mapping of chemical information at atomic resolution. Phys Rev Lett 99:086102

Brydson R (2001) Electron Energy-loss Spectroscopy. BIOS (now Taylor Francis), Oxford.

Brydson R (ed) (2011) Aberration-Corrected Analytical Transmission Electron Microscopy. Wiley, West Sussex

Brydson R, Sauer H, Engel W, Thomas JM, Zeitler E (1989) Coordination fingerprints in electron loss near-edge structures - determination of the local site symmetry of aluminum and beryllium in ultrafine minerals. J Chem Soc Chem Comm 1989:1010-1012, doi: 10.1039/C39890001010

Brydson R, Williams BG, Engel W, Lindner T, Muhler M, Schlogl R, Zeitler E, Thomas JM (1988) Electron energy-loss spectroscopy and the crystal-chemistry of rhodizite: near-edge structure. J Chem Soc Farad Trans 1 84:631-646

Buatier MD, Guillaume D, Wheat CG, Hervé L, Adatte T (2004) Mineralogical characterization and genesis of hydrothermal Mn oxides from the flank of the Juan the Fuca Ridge. Am Mineral 89:1807-1815.

Burke IT, Livens FR, Lloyd JR, Brown A, Law GTW, McBeth JM, Ellis B, Lawson RS, Morris K (2010) Fate of technetium in reduced sediments: comparison of direct and indirect analysis. Appl Geochem 25(2):233-241

Burke IT, Mayes WM, Peacock CL, Brown AP, Jarvis AP, Gruiz K (2012) Speciation of arsenic, chromium and vanadium in red mud samples from the Ajka spill site, Hungary. Environ Sci Technol 46:3085-3092

Calvert CC, Brown A, Brydson R (2005) Determination of the local chemistry of iron in inorganic and organic materials. J Electron Spectrosc Relat Phenom 143:173

Calvert CC, Gutzmer J, Banks DA and Rainforth WM (2008) EELS characterisation and valence determination of Mn minerals from the Kalahari Manganese Field in South Africa. J Phys Conf Ser 126:012045

Champness PE (1977) Transmission electron microscopy in earth science. Ann Rev Earth Planet Sci 5:203-226

Clark SJ, Segall MD, Pickard CJ, Hasnip PJ, Probert MJ, Refson K, Payne MC (2005) First principles methods using CASTEP. Z Kristallogr 220:567-570. See also http://www.castep.org/

Csákberényi-Malasics D, Rodriguez-Blanco JD, Rečnik A, Benning LG, Pósfai M (2012) Structural properties and transformations of precipitated FeS. Chem Geol 294-295:249-258

D'Alfonso AJ, Freitag B, Klenov D, Allen LJ (2010) Atomic-resolution chemical mapping using energy-dispersive X-ray spectroscopy. Phys Rev B 81:100101

Daniels H, Brydson R, Rand B, Brown A (2007) Investigating carbonization and graphitization using electron energy loss spectroscopy (EELS) in the transmission electron microscope (TEM). Philos Mag 87:4073-4092

de Groot F, Kotani A (2008) Core Level Spectroscopy of Solids. Taylor & Francis CRC press.

Drits VA, Sakharov BA, Salyn AL, Manceau A (1993) Structural model for ferrihydrite. Clay Miner 28:185-207

Drummond-Brydson RM, Sauer H, Engle W (2004) Probing Materials Chemistry Using ELNES. In: Transmission Electron Energy Loss Spectrometry in Materials Science and The EELS Atlas, 2nd Edition. Ahn CC (ed) Wiley-VCH Verlag GmbH & Co., p 223-270

Eddisford P, Brown A, Brydson R (2007) Identifying and quantifying the mechanism of electron beam induced damage and recovery in hydroxyapatite. J Phys Conf Ser 126:12008

Egerton RF (2011) Electron Energy-loss spectroscopy in the Electron Microscope (3rd Edition). Springer, New York.

Egerton RF, Li P, Malac M (2004) Radiation damage in the TEM and SEM. Micron 35:399-409

Egerton RF, McLeod R, Wang F, Malac M (2010) Basic questions related to electron-induced sputtering in the TEM. Ultramicroscopy 110:991-997

Engel W, Sauer H, Zeitler E, Brydson R, Williams BG, Thomas JM (1988) Electron energy-loss spectroscopy and the crystal-chemistry of rhodizite. 1. Instrumentation and chemical-analysis. J Chem Soc Farad Trans 1 84:617-629

Fredrickson JK, Zachara JM, Kennedy DW, Liu C, Duff MC, Hunter DB, Dohnalkova A (2002) Influence of Mn oxides on the reduction of uranium(VI) by the metal-reducing bacterium *Shewanella putrefaciens*. Geochim Cosmochim Acta 66:3247-3262

Gai PL (2007) *In situ* environmental transmission electron microscopy. *In:* Nanocharacterisation. Hutchison AI, Kirkland JL (eds) RCS Publishing, p 268-290

Garvie LAJ, Craven AJ (1994a) High-resolution parallel electron energy-loss spectroscopy of Mn $L_{2,3}$-edges in inorganic manganese compounds. Phys Chem Miner 21:191-206

Garvie LAJ, Craven AJ (1994b) Electron-beam-induced reduction of Mn4+ in manganese oxides as revealed by parallel EELS. Ultramicroscopy 54:83-92

Garvie LAJ, Craven AJ, Brydson R (1994) Use of electron energy-loss near-edge fine structure in the study of minerals. Am Mineral 79:411-425

Garvie LAJ, Zega TJ, Rez P, Buseck PR (2004) Nanometer-scale measurements of $Fe^{3+}/\Sigma Fe$ by electron energy-loss spectroscopy; a cautionary note. Am Mineral 89:1610-1616

Giannuzzi LA (ed) (2004) Introduction to Focused Ion Beams: Instrumentation, Theory, Techniques and Practice. Springer

Glatzel P, Bergmann U, Yano J, Visser H, Roblee JH, Gu W, de Groot FMF, Christou G, Pecoraro VL, Cramer SP, Yachandra VK (2004) The electronic structure of Mn in oxides, coordination complexes, and the oxygen-evolving complex of photosystem II studied by resonant inelastic X-ray scattering. J Am Chem Soc 126: 9946-9959

Goodhew PJ, Humphreys FJ, Beanland R (2001) Electron Microscopy and Analysis. Taylor and Francis

Guyodo Y, Sainctavit P, Arrio MA, Carvallo C, Penn RL, Erbs JJ, Forsberg BS, Morin G, Maillot F, Lagroix F, Bonville P, Wilhelm F, Rogalev A (2012) X-ray magnetic circular dichroism provides strong evidence for tetrahedral iron in ferrihydrite. Geochem Geophys Geosyss 13:1525-2027

Harrington R, Hausner DB, Xu W, Bhandari N, Michel FM, Brown Jr GE, Strongin DR, Parise JB (2011) Neutron pair distribution function study of two-line ferrihydrite. Environ Sci Technol 45:9883-9890

Hawkes PW (ed) (2008) Advances in Imaging and Electron Physics, Volume 153. Elsevier

Haynes BW, Law SL, Barron DC, Kramer GW, Maeda R, Magyar MJ (1985) Pacific manganese nodules: Characterization and processing. Bulletin of the Department of the Interior, Bureau if Mines 679:43

Hewett DF, Fleischer M (1960) Deposits of manganese oxides. Econ Geol 55:1-55

Hillier S, Lumsdon DG, Paterson E, Brydson R (2007) Hydrogarnet: A host phase for Cr(VI) in chromite ore processing residue (COPR) and other high pH wastes. Environ Sci Technol 41:1921-1927

Hobbs LW (1987) Radiation effects in analysis by TEM. *In*: Introduction to Analytical Electron Microscopy. Hren JJ, Goldstein JI, Joy DC (eds) Plenum Press, New York, p 399-445

Hochella MF Jr, Moore JN, Golla U, Putnis A (1999) A TEM study of samples from acid mine drainage systems: Metal-mineral association with implications for transport. Geochim Cosmochim Acta 63:3395-3406

Hofer F, Wilhem P (1993) EELS microanalysis of the elements Ca to Cu using $M_{2,3}$ edges. Ultramicroscopy 49:189-197

Hondow N, Brydson R, Brown A, Wang P, Holton MD, Brown MR, Rees P, Summers HD (2012) Quantitative characterization of nanoparticle agglomeration within biological media. J Nanopart Res 14:977-991

Huebner JS (1976) The manganese oxides – a bibliographic commentary. Rev Mineral 3:SH-1–SH-17

Hutchison JL, Kirkland AI (2007) Nanocharacterisation. Royal Society of Chemistry, London.

Ishitani T, Tsuboi H, Yaguchi T, Koike H (1994) Transmission electron microscope sample preparation using focused ion beam. J Electron Microsc 43:322-326

Kim B, Park C-S, Murayama M, Hochella MF Jr (2010) Discovery and characterization of silver sulfide nanoparticles in final sewage sludge products. Environ Sci Technol 44:7509-7514

Klein KL, Anderson IM, De Jonge N (2011) Transmission electron microscopy with a liquid flow cell. J Microscopy 242:117-123

Kurata H, Colliex C (1993) Electron-energy-loss core-edge structures in manganese oxides. Phys Rev B 48:2102-2108

Kurata H, Lefevre E, Colliex C, Brydson R (1993) Electron-energy-loss near-edge structures in the oxygen k-edge spectra of transition-metal oxides. Phys Rev B 47:13763-13768

Laffont L, Gibot P (2010) High resolution electron energy loss spectroscopy of manganese oxides: Application to Mn_3O_4 nano particles. Mater Charact 61:1268-1273

Leapman RD, Grunes LA (1980) White-line ratios in the 3d transition metals. Phys Rev Lett 45:397-401.

Lear G, McBeth JM, Boothman C, Gunning DJ, Ellis B, Lawson R, Morris K, Burke, IT, Bryan N, Livens FR, Lloyd JR (2010) Probing the biogeochemical behavior of technetium using a novel nuclear imaging approach. Environ Sci Technol 44:156-162

Leary R, Brydson R (2011) Chromatic aberration correction: the next step in electron microscopy. Adv Imag Elect Phys 165:73-130

Lee M (2010) Transmission electron microscopy (TEM) of earth and planetary materials: a review. Mineral Mag 74(1):1-27

Lee MR, Brown DJ, Smith CL, Hodson ME, MacKenzie M, Hellmann R (2007) Characterization of mineral surfaces using FIB and TEM: A case study of naturally weathered alkali feldspars. Am Mineral 92:1383-1394

Levard C, Reinsch BC, Michel FM, Oumahi C, Lowry GV, Brown GE Jr (2011) Sulfidation processes of PVP-coated silver nanoparticles in aqueous solution: impact on dissolution rate. Environ Sci Technol 45:5260-5266

Livi KJT, Christidis G, Árkai P, Veblen DR (2008) White mica domain formation: A model for paragonite, margarite, and muscovite formation during prograde metamorphism. Am Mineral 92:1288-1302

Livi KJT, Lafferty B, Zhu M, Zhang S, Gaillot A-C, Sparks DL (2012) Electron energy-loss safe-dose limits for manganese valence measurements in environmentally relevant manganese oxides. Environ Sci Technol 46:970-976

Loomer DB, Al TA, Weaver L, Cogswell S (2007) Manganese valence imaging in Mn minerals at the nanoscale using STEM-EELS. Am Mineral 92:72-79

Luo W, Varela M, Tao J, Pennycook SJ, Pantelides ST (2009) Electronic and crystal-field effects in the fine structure of electron energy-loss spectra of manganites. Phys Rev B 79:052405

Ma C, Fitzgerald JD, Eggleton RA, Llewellyn DJ (1998) Analytical electron microscopy in clays and other phyllosilicates: Loss of elements from a 90-nm stationary beam of 300-keV electrons. Clays Clay Miner 46:301-316

Maillot F, Morin G, Wang Y, Bonnin D, Ildefonse P, Chaneac C, Calas G (2011) New insight into the structure of nanocrystalline ferrihydrite: EXAFS evidence for tetrahedrally coordinated iron(III). Geochim Cosmochim Acta 75:2708-2720

Manceau A (2009) Evaluation of the structural model for ferrihydrite derived from real space modeling of high energy X-ray diffraction data. Clay Miner 44:19-34

Manceau A (2010) PDF analysis of ferrihydrite and the violation of Pauling's Principia. Clay Miner 45:225-228

Manceau A (2011) Critical evaluation of the revised akdalaite model for ferrihydrite. Am Mineral 96:521-533

Manceau A (2012) Critical evaluation of the revised akdalaite model for ferrihydrite—Reply. Am Mineral 97:255-256

Manceau A, Drits VA, Silvester E, Bartoli C, Lanson B (1997) Structural mechanism of Co^{2+} oxidation by the phyllomanganate buserite. Am Mineral 82:1150-1175

Mansot JL, Leone P, Euzen P, Palvadeau P (1994) Valence of manganese, in a new oxybromide compound, determined by means of electron energy loss spectroscopy. Microsc Microanal Microstruct 5:79-90

Merriman RJ, Peacor DR (1999) Very low-grade metapelites: mineralogy, microfabrics and measuring reaction progress. *In:* Low-Grade Metamorphism. Frey M, Robinson D (eds) Blackwell Science Ltd, Oxford, p 10-60

Michel FM, Ehm L, Antao SM, Lee PL, Chupas PJ, Liu G, Strongin DR, Schoonen MAA, Phillips BL, Parise JB (2007) The structure of ferrihydrite, a nanocrystalline material. Science 316:1726-1729

Michel FM, Barron V, Torrent J, Morales MP, Serna CJ, Boily J-F, Liu Q, Ambrosini A, Cismasu AC, Brown GE (2010) Ordered ferrimagnetic form of ferrihydrite reveals links among structure, composition, and magnetism. Proc Nat Acad Sci 107:2787-2792

Morello M, Canini A, Mattioli P, Sorge RP, Alimonti A, Bocca B, Forte G, Martorana, A, Bernardi G, Sancesario G (2008) Sub-cellular localization of manganese in the basal ganglia of normal and manganese-treated rats: An electron spectroscopy imaging and electron energy-loss spectroscopy study. NeuroToxicol 29:60-72

Murray JW, Dillard JG (1979) Oxidation of cobalt (II) adsorbed on manganese-dioxide. Geochim Cosmochim Acta 43:781-787

Obst M, Gasser P, Mavrocordatos D, Dittrich M (2005) TEM-specimen preparation of cell/mineral interfaces by focused ion beam milling. Am Mineral 90:1270-1277

Oscarson DW, Huang PM, Defosse C, Herbillon A (1981) Oxidative power of Mn(IV) and Fe(III) oxides with respect to As(III) in terrestrial and aquatic environments. Nature 291:50-51

Otten MT, Miner B, Rask JH, Buseck PR (1985) The determination of Ti, Mn and Fe oxidation states in minerals by electron energy-loss spectroscopy. Ultramicroscopy 18:285-290

Pan Y, Brown A, Brydson R, Warley A, Li A, Powell J (2006) Electron beam damage studies of synthetic 6-line ferrihydrite and ferritin molecule cores within a human liver biopsy. Micron 37:403-411

Pan YH, Brown A, Sader K, Brydson R, Gass M, Bleloch A (2008) Quantification of absolute iron content in mineral cores of cytosolic ferritin molecules in human liver. Mater Sci Technol Lond 24(6):689-694

Pan YH, Sader K, Powell J, Bleloch A, Gass M, Trinick J, Warley A, Li A, Brydson R, Brown A (2009) Atomically resolved in situ quantitative analytical electron microscopy of human hepatic ferritin mineral**.** J. Struct Biol 166(1):22-31

Pan YH, Vaughan G, Brydson R, Bleloch A, Gass M, Sader K, Brown A (2010) Electron-beam-induced reduction of Fe^{3+} in iron phosphate dihydrate, ferrihydrite, haemosiderin and ferritin as revealed by electron energy-loss spectroscopy. Ultramicroscopy 110:1020-1032

Patterson JH, Krivanek OL (1990) ELNES of 3*d* transition-metal oxides II: Variations with oxidation state and crystal structure. Ultramicroscopy 32:319-325

Peak D, Regier T (2012) Direct observation of tetrahedrally coordinated Fe(III) in ferrihydrite. Environ Sci Technol 46:3163-3168

Pearson DH, Ahn CC, Fultz B (1993) White lines and d-electron occupancies for the 3d and 4d transition metals. Phys Rev B 47:8471

Pecher K, McCubbery D, Kneedler E, Rothe J, Bargar J, Meigs G, Cox L, Nealson K, Toner B (2003) Quantitative charge state analysis of manganese biominerals in aqueous suspension using Scanning Transmission X-ray Microscopy (STXM). Geochim Cosmochim Acta 67:1089-1098

Penn RF, Banfield JF (1998) Imperfect oriented attachment: Dislocation generation in defect-free nanocrystals. Science 281:969

Post JE (1999) Manganese oxide minerals: Crystal structures and economic and environmental significance. Proc Natl Acad Sci USA 96:3447-3454

Raiswell R, Tranter M, Benning LG, Siegert M, De'ath R, Huybrechts P, Payne T (2006) Contributions from glacially derived sediment to the global iron (oxyhydr)oxide cycle: Implications for iron delivery to the oceans. Geochim Cosmochim Acta 70:2765-2780

Rancourt DG, Meunier J-F (2008) Constraints on structural models of ferrihydrite as a nanocrystalline material. Amer Mineral 93:1412-1417

Rask JH, Miner BA, Buseck PR (1987) Determination of manganese oxidation states in solids by electron energy-loss spectroscopy. Ultramicroscopy 21:321-326

Reidl T, Gemming T, Wetzig K (2006) Extraction of EELS white-line intensities of manganese compounds: Methods, accuracy, and valence sensitivity. Ultramicroscopy 106:284-291

Reimer L, Kohl H (2008) Transmission Electron Microscopy. Springer -Verlag, Berlin.

Richman JD, Livi KJT, Geyh AS (2011) A scanning transmission electron microscopy method for determining manganese composition in welding fume as a function of primary particle size. J Aerosol Sci 42:408-418

Rodriguez-Blanco JD, Shaw S, Benning LG (2008) How to make 'stable' ACC: protocol and structural characterization. Mineral Mag 72(1):283-286

Rodríguez-Blanco JD, Shaw S, Benning LG (2011) The kinetics and mechanisms of amorphous calcium carbonate (ACC) crystallization to calcite, via vaterite. Nanoscale 3:265-271

Roy S (1968) Mineralogy of different genetic types of manganese deposits. Econ Geol 63:760-786

Sader K**,** Schaffer B, Vaughan G, Brydson R, Brown A, Bleloch A (2010) Smart acquisition EELS. Ultramicroscopy 110:998-1003

Sauer H, Brydson R, Rowley PN, Engel W, Thomas JM (1993) Determination of coordinations and coordination-specific site occupancies by electron energy-loss spectroscopy - an investigation of boron oxygen compounds. Ultramicroscopy 49:198-209

Schaffer M, Schaffer B, Ramasse Q (2012) Sample preparation for atomic-resolution STEM at low voltages by FIB. Ultramicroscopy 114:62-71

Schmidt D, Livi KJT, Frey M (1999) Reaction progress in chloritic material: an electron microbeam study of the Taveyanne greywacke, Switzerland. J Metamorph Geol 17:229-241

Schmidt HK, Mader W (2006) Oxidation states of Mn and Fe in various compound oxide systems. Micron 37:426-432

Schwarz K, Blaha P, Madsen GKH (2002) Electronic structure calculations of solids using the WIEN2k package for material sciences. Comput Phys Commun 147:71-76. See also *http://www.wien2k.at/*

Scott AJ, Brydson R, MacKenzie M, Craven AJ (2001) A theoretical investigation of the ELNES of transition metal carbides and nitrides for the extraction of structural and bonding information. Phys Rev B 63:245105

Sparrow TG, Williams BG, Rao CNR, Thomas JM (1984) L_3/L_2 whiteline intensity ratios in the electron energy-loss spectra of 3d transition-metal oxides. Chem Phys Lett 108:547-550

Stolojan V, Walsh C, Yuan J, Brown L (1999) Calibration of the relationship between white-line intensity and valence states for the first transition series. In: Electron Microscopy and Analysis 1999: Proceedings of the Institute of Physics Electron Microscopy and Analysis Group Conference, University of Sheffield, 24-27 August 1999. Kiely CJ (ed) CRC Press. Inst Phys Conf Ser 161:235-237

Suzuki Y, Kelly SD, Kemner KM, Banfield JF (2002) Radionuclide contamination - Nanometre-size products of uranium bioreduction. Nature 419:134-134

Tobler DJ, Shaw S, Benning LG (2009) Quantification of initial steps of nucleation and growth of silica nanoparticles: an *in situ* SAXS and DLS study. Geochim Cosmochim Acta 73(18)5377-5393

Utsunomiya S, Ewing RC (2003) Application of high-angle annular dark field scanning transmission electron microscopy (HAADF-STEM), STEM-energy dispersive X-ray spectrometry (EDX), and energy-filtered (EF)-TEM to the characterization of nanoparticles in the environment. Environ Sci Technol 37:786-791

Utsunomiya S, Kersting AB, Ewing RC (2009) Groundwater nanoparticles in the far-field at the Nevada Test Site: mechanism for radionuclide transport. Environ Sci Technol 43:1293-1298

van Aken PA, Styrsa VJ, Liebscher B, Woodland AB, Redhammer GJ (1999) Microanalysis of $Fe^{3+}/\Sigma Fe$ in oxide nad silicate minerals by investigation of electron energy-loss near-edge structures (ELNES) at the Fe $M_{2,3}$ edge. Phys Chem Miner 26:584-590

van Cappellen EV, Doukhan J-C (1994) Quantitative transmission X-ray micro-analysis of ionic compounds. Ultramicroscopy 53:343-349

Van Driessche AES, Benning LG, Rodriguez-Blanco JD, Ossorio M, Bots P, García-Ruiz JM (2012) The role and implications of bassanite as a stable precursor phase to gypsum precipitation. Science 336:69-72

Varella M, Oxley MP, Luo W, Tao J, Watanabe M, Lupini AR, Pantelides ST, Pennycook SJ (2009) Atomic-resolution imaging of oxidation states in manganites. Phys Rev B 79:085117

Vaughan G, Brydson R, Brown A (2012) Characterisation of synthetic two-line ferrihydrite by electron energy loss spectroscopy. J Phys Conf Ser 371:12079

Ward MB, Kapitulčinová D, Brown AP, Heard PJ, Cherns D, Cockell CS, Hallam KR, Ragnarsdóttir KV (2013) Investigating the role of microbes in mineral weathering: Nanometer-scale characterisation of the cell-mineral interface using FIB and TEM. Micron 47:10-17; doi: *http://dx.doi.org/10.1016/j.micron.2012.12.006*

Watanabe M (2009) Atomic-resolution chemical analysis by electron energy-loss spectrometry and X-ray energy dispersive spectrometry in aberration-corrected electron microscopy. *In:* Proceedings of the 7th International Symposium on Atomic Level Characterizations for New Materials and Devices '09 (ALC'09). The 141st Committee on Microbeam Analysis of Japan Society for the Promotion of Science, p 400-405

Weyland M, Midgley PA (2007) Electron tomography. *In:* Nanocharacterisation. Hutchison AI, Kirkland JL (eds) RCS Publishing, p 184-267

White KN, Ejim AI, Walton RC, Brown AP, Jugdaohsingh R, Powell JJ, McCrohan CR (2008) Avoidance of aluminum toxicity in freshwater snails involves intracellular silicon-aluminum bio-interaction. Environ Sci Technol 42(6): 2189-2194

Whittleston RA, Stewart DI, Mortimer RJG, Tilt ZC, Brown AP, Geraki K, Burke IT (2011) Chromate reduction in Fe(II)-containing soil affected by hyperalkaline leachate from chromite ore processing residue. J Hazard Mater 194:15-23

Williams DB, Carter CB (2009) Transmission Electron Microscopy. Plenum Press, New York

Xu W, Hausner DB, Harrington R, Lee PL, Strongin DR, Parise JB (2011) Structural water in ferrihydrite and constraints this provides on possible structure models. Amer Mineral 96:513-520

Zhang S, Livi KJT, Gaillot A-C, Stone AT, Veblen DR (2010) Determination of manganese valence states in (Mn^{3+}, Mn^{4+}) minerals by electron energy-loss spectroscopy. Am Mineral 95:1741-1746